A Measurement of the Azimuthal Decorrelation in Di-Jet Events in Proton-Proton Collisions at $\sqrt{s} = 7\,\text{TeV}$ at the Large Hadron Collider

by

Gabriel Rosenbaum

A thesis submitted in conformity with the requirements
for the degree of Doctor of Philosophy
Graduate Department of Physics
University of Toronto

Abstract

A Measurement of the Azimuthal Decorrelation in Di-Jet Events in Proton-Proton Collisions at $\sqrt{s} = 7\,\text{TeV}$ at the Large Hadron Collider

Gabriel Rosenbaum

Doctor of Philosophy

Graduate Department of Physics

University of Toronto

2011

A measurement of the azimuthal decorrelation in di-jet events in proton-proton collisions at $\sqrt{s} = 7\,\text{TeV}$ is presented. Using $19.6\,\text{nb}^{-1}$ of data collected in the ATLAS detector this measurement uses the angle ($\Delta\phi$) in the transverse plane between the two leading p_T jets to measure the normalized differential cross section $\frac{1}{\sigma_{tot}}\frac{d\sigma}{d(\Delta\phi)}$. An unfolding correction is a applied to give a jet-level result. The unfolded spectrum is compared to the predictions of two Monte Carlo event generators: Pythia and Herwig++.

Contents

List of Tables

List of Figures

Chapter 1

Introduction

This thesis describes a measurement made using the ATLAS detector at the Large Hadron Collider (LHC). The measurement of interest is the azimuthal decorrelation in di-jet events. This introductory chapter lays out some of the theoretical background needed to understand this measurement, discusses some of the details of the high energy physics entities known as "jets" and describes and motivates the measurement. Chapter 2 gives an overview of the LHC and describes the ATLAS detector. Chapter 3 details the algorithms used by the analysis software which use detector output to reconstruct jets. Details of the data set and a simulated data set are discussed in chapter 4. The details of this specific analysis are explained in chapter 5 including discussions of uncertainty calculations. The results are shown with a comparison to simulation predictions in chapter 6. Concluding remarks can be found in chapter 7.

The remainder of this chapter is a synthesis of ideas taken from [1][2][3][4][5][6].

1.1 The Standard Model

The Standard Model (SM) of particle physics is a theory that describes the particles which make up all matter that we know of and the interactions, or forces, between these particles. There are three fundamental forces described by the SM which are: the electromagnetic force, the weak force and the strong force. The SM is based on a gauge symmetry under the group $U_Y(1)\otimes SU_L(2)\otimes SU_C(3)$. The group $U_Y(1)\otimes SU_L(2)$ yields the electroweak (the unified electromagnetic and weak) forces while the group $SU_C(3)$ describes the strong interactions. The SM says nothing of the gravitational interaction; however, the gravitational force is so weak (at currently accessible energy scales) compared to the other forces that it is neglected in the following without consequence.

The SM includes two classes of particles, these are the fermions which are spin-$\frac{1}{2}$* and, bosons which are particles with integer spin. The vector bosons (spin-1) in the SM mediate the interactions of the particles, including in some cases the interactions of the bosons with themselves, by transmitting the force between them. The force carrying boson for the electromagnetic force is the photon. The vector bosons of the weak interaction are the $W^{\pm}$ and the Z^0, and there are eight gluons that transmit the strong force.

There is one additional boson (which is spin-0) in the SM called the Higgs boson. This particle is a result of the Higgs mechanism which is needed in the SM in order to generate particle masses. The Higgs mechanism involves introducing a SU(2) complex

*In general fermions can be any be any half integer spin (e.g. $\frac{1}{2}, \frac{3}{2}, \frac{5}{2}\ldots$) but the fundamental fermions of the SM are spin-$\frac{1}{2}$.

scalar doublet field into the theory and allows particles to have mass in the theory without violating gauge invariance. The result is that the theory requires one spin-0 particle which couples to all massive particles. This is the Higgs boson; which is the only SM particle yet to be discovered experimentally.

The fundamental fermions are the building blocks of matter. They are classified in two groups: leptons and quarks. Both the leptons and the quarks are grouped into three generations where each generation contains a SU(2) doublet of particles giving a total of six leptons and six quarks. Each lepton doublet contains one particle with charge -1; these three leptons are (in order of increasing mass): the electron (e), muon (μ) and tau (τ), each having a corresponding (electric) chargeless neutrino, (ν_e, ν_μ and ν_τ respectively). The lepton generations differ in mass[†] and can be written in ascending mass order as:

$$\begin{pmatrix} e \\ \nu_e \end{pmatrix} \qquad \begin{pmatrix} \mu \\ \nu_\mu \end{pmatrix} \qquad \begin{pmatrix} \tau \\ \nu_\tau \end{pmatrix}.$$

The quarks are named up (u), down (d), charm (c), strange (s), top (t) and bottom (b) and are written in their doublets, in ascending mass order as:

$$\begin{pmatrix} u \\ d \end{pmatrix} \qquad \begin{pmatrix} c \\ s \end{pmatrix} \qquad \begin{pmatrix} t \\ b \end{pmatrix}.$$

The quark charges are $+\frac{2}{3}$ for the up-type (the upper entry in the doublet) or $-\frac{1}{3}$ for the down-type (lower entry).

The leptons do not combine with other particles to form other subatomic particles.

[†]The mass referred to here are the masses of the e, μ and τ. The neutrinos also have mass (although they are treated as massless in the SM) but their masses are not known at this time.

However, the contrary is true for the quarks whereby they do not exist in a bare state (alone) but rather combine to form what are known as hadrons. Hadrons are classified as either baryons or mesons. Baryons contain three quarks whose electric charges sum to an integer value, for example the proton (uud) and the neutron (udd). Mesons contain one quark and one anti-matter partner of the quark, the anti-quark, for example pions (e.g. $u\bar{u}$ or $u\bar{d}$).

It is the strong force that is of interest in the following discussion as it is the interaction which is relevant to the physics studied in this thesis. This is the force which is responsible for holding protons and neutrons together in atomic nuclei and is also the force with which the constituents of the proton interact most readily[‡].

1.2 Quantum Chromodynamics

The theory of the strong force is known as quantum chromodynamics (QCD) and is based on the gauge symmetry $SU_C(3)$, where C stands for colour. The requirement of local gauge invariance under $SU(3)$ transformations results in eight massless gluons which carry colour charge (of which there are three, and three anti-charges) and are responsible for the transmission of this force. There are three interaction vertices in QCD which are shown in figure 1.1 along with the corresponding dependence on α_s, the coupling strength of the strong interaction. The convention used for the Feynman diagrams to depict quarks and gluons is also shown and labelled. Note that in QCD the force carrying bosons (the gluons) have self-interactions, which will be important

[‡]In fact the constituents of the proton can interact via the electromagnetic and weak forces as well but, as the name implies, the strong force is much stronger and dominates other interactions.

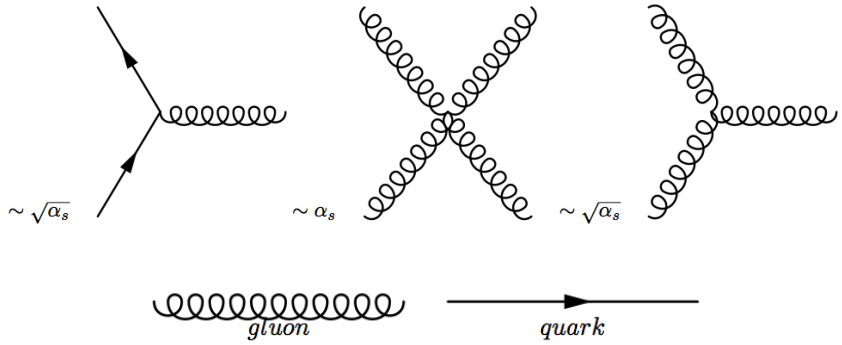

Figure 1.1: The possible QCD vertices with order in α_S shown. The convention used for the Feynman diagram depiction of quarks and gluons is also shown and labelled.

in following section.

1.2.1 Running of α_s

The strength of the strong interaction depends on a parameter, α_s, which depends on the four momentum transfer (Q^2) between the interacting partons. In order to understand this phenomenon qualitatively it is useful to first consider a similar phenomenon in the theory of quantum electrodynamics (QED), which describes the electromagnetic interaction. In QED the force carrying boson (the photon) couples to electrically charged particles. Since the photon does not carry electric charge it does not couple to itself, therefore the only vertex possible is the one analogous to the left most diagram in figure 1.1 with $q \to e$, $g \to \gamma$ and with the coupling $\alpha_S \to \alpha$ where α is the strength of the QED coupling. In the case of $e^+e^- \to e^+e^-$ (Bhabha) scattering[§], the leading order diagram can be modified by diagrams in which the photon contains

[§]Bhabha scattering is one example, the situation is the same regardless of the process in which the photon is exchanged.

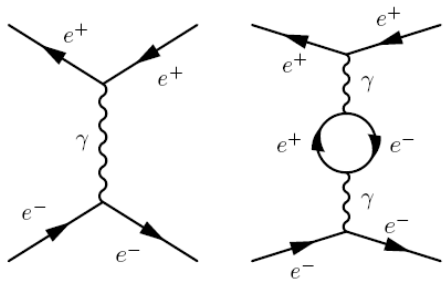

Figure 1.2: Example of a leading order and a next to leading order $e^+e^- \rightarrow e^+e^-$ Feynman diagram.

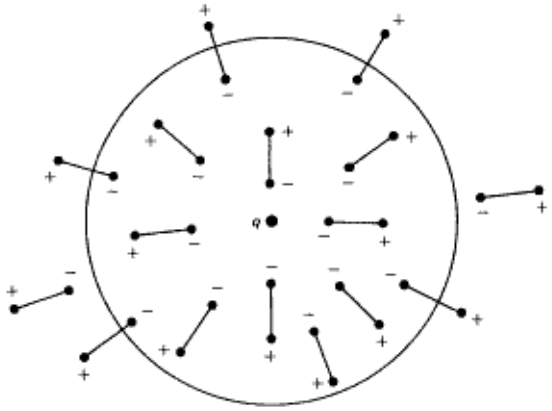

Figure 1.3: Schematic diagram of screening due to dipoles in a dielectric medium.

intermediate e^+e^- loops. Figure 1.2 shows an example of a leading order (LO) and a next to leading order (NLO) contributions to Bhabha scattering. The effect of having the e^+e^- loop is similar to the charge screening due to dipoles around an electric charge in a dielectric medium, as illustrated in figure 1.3, where the perceived charge increases with shorter distance to the charge. Short distance scale equates to higher Q^2 meaning that the QED coupling increases with Q^2.

In QCD a similar effect is present, however there are more possible vertices to consider. In the case in which only quark loops are considered, the same effect as the

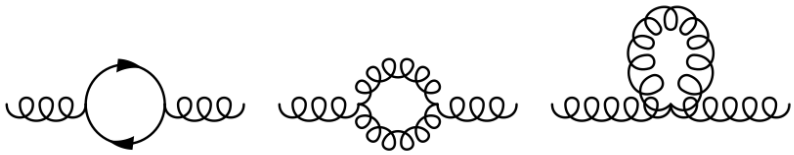

Figure 1.4: Possible loops in the gluon propagator which are responsible for colour charge screening and anti-screening.

QED screening occurs. However, since the gluon itself carries colour charge the gluon self-interactions add two extra corrections with gluon loops, at leading order. Figure 1.4 shows the three types of loops in the gluon propagator which go into the effect on the strong coupling. Unlike the quark loop which leads to colour charge screening analogous to the electric charge screening of QED, the gluon loops have an anti-screening effect that decreases the coupling with increasing Q^2. The overall dependence of α_S on Q^2 (at LO) is

$$\alpha_s(Q^2) = \frac{12\pi}{(11n - 2f)\ln\frac{Q^2}{\Lambda^2}} \tag{1.1}$$

where n is the number of colours, f is the number of quark flavours and Λ is the energy scale, such that this evolution is only valid for $Q^2 \gg \Lambda^2$. From equation 1.1 it is clear that with increasing Q^2, α_s decreases. Figure 1.5 shows recent measurements of, and fits to, α_s as a function of Q^2[7].

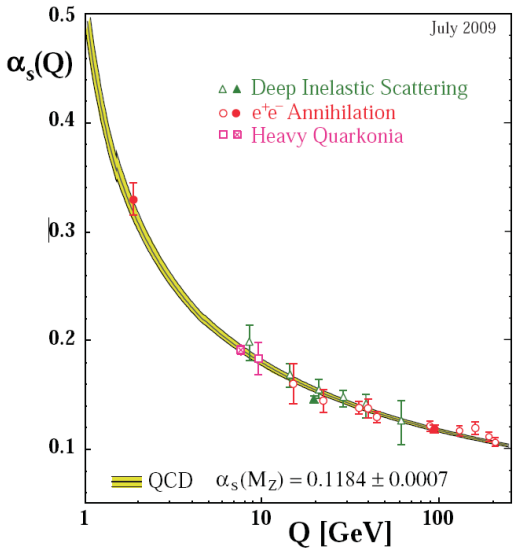

Figure 1.5: Running of α_s as a function of Q^2.

1.3 Factorization

The problem of calculating what happens when two protons are brought into collision at high energies is very complex. It involves QCD physics at many different scales and hence different values of α_s. The quarks inside a single proton interact with each other at low energy or large distance ($\sim$ 1 fm), while the interaction between the constituents of the two colliding protons happens at high energy or short distance scale. The fate of the final state particles from that interaction is also governed by large distance scale QCD. Because α_s decreases with increasing energy, the hard interaction of the partons can be calculated by means of a perturbative expansion since the coupling is small. However, the initial and final processes, which take place at large distance scale, are not calculable perturbatively, so the full interaction can not be calculated. Fortunately, according to the factorization theorem[8], these three processes can be treated independently; a perturbative calculation can be used for

the hard interaction of the partons while other methods are used to handle the large distance scale physics describing the initial and final states. Explicitly, the cross section for an interaction of two partons, a and b coming from protons A and B, interacting and producing some partonic final state X can be written as[¶]

$$\sigma_{AB} = \int dx_a dx_b \, f_{a/A}(x_a) f_{b/B}(x_b) \hat{\sigma}_{ab\to X} \; . \tag{1.2}$$

Here the functions $f_{a/A}(x_a)$ and $f_{b/B}(x_b)$ are parton density functions describing the distribution of the momentum fraction x_a (or x_b) of the initial state partons in a proton, and $\hat{\sigma}_{ab\to X}$ is the cross section of the hard interaction $ab \to X$ which is calculable perturbatively. What happens to the outgoing partons is then treated separately as described in section 1.3.3. This splitting of the entire process into three sub-processes is called factorization and is needed to make predictions at the LHC. Note that there is one other part of the process which is not mentioned in the above. This related to the remaining part of the proton which was not involved in the hard interaction. This is known as the underlying event. It is also described by large distance scale physics and can be accounted for by means of a correction to measured quantities.

1.3.1 Parton Density Functions

The parton density functions (PDFs) $f_{a/A}(x_a)$ and $f_{b/B}(x_b)$ in equation 1.2 are used to calculate the probability of having some type of parton carrying a fraction x of

[¶]In general the process does not have to be parton-parton → n-partons but for the purpose of this thesis it is the process of concern.

the total proton momentum. PDFs cannot be calculated from first principles but rather are determined from fits to experimental results, for example, deep inelastic scattering of electrons and protons and the results of hadron collider experiments. The two most prevalent collaborations which provide PDFs are the CTEQ[9] and MRST[10] groups. The PDFs mentioned above, however, are an over-simplification. In fact, PDFs have a dependence on the momentum transfer, Q^2, between the initial state partons. This is due to the fact that before the interaction the incoming partons can emit initial state radiation (ISR), that is, emit another parton in a splitting as illustrated in the diagrams shown in figure 1.6. The PDFs evolve as a function of Q^2 according to the Dokshitzer - Gribov - Lipatov - Altarelli - Parisi (or DGLAP) equations[11], which are

$$\begin{aligned}
\frac{dq(x,Q^2)}{d\log Q^2} &= \frac{\alpha_s}{2\pi}\int_x^1 \frac{dy}{y}\left(P_{q\leftarrow q}\left(\frac{x}{y}\right)\cdot q(y,Q^2) + P_{q\leftarrow g}\left(\frac{x}{y}\right)\cdot g(y,Q^2)\right)\\
\frac{d\bar{q}(x,Q^2)}{d\log Q^2} &= \frac{\alpha_s}{2\pi}\int_x^1 \frac{dy}{y}\left(P_{q\leftarrow q}\left(\frac{x}{y}\right)\cdot \bar{q}(y,Q^2) + P_{q\leftarrow g}\left(\frac{x}{y}\right)\cdot g(y,Q^2)\right)\\
\frac{dg(x,Q^2)}{d\log Q^2} &= \frac{\alpha_s}{2\pi}\int_x^1 \frac{dy}{y}\left(P_{g\leftarrow q}\left(\frac{x}{y}\right)\cdot \sum_q \left[q(y,Q^2)+\bar{q}(y,Q^2)\right] + P_{g\leftarrow g}\left(\frac{x}{y}\right)\cdot g(y,Q^2)\right)
\end{aligned} \tag{1.3}$$

where the PDFs have been split up into $q(x,Q^2)$, $\bar{q}(x,Q^2)$ and $g(x,Q^2)$ for quarks, anti-quarks and gluons respectively[‖]. The functions of the form $P_{p\leftarrow p'}\left(\frac{x}{y}\right)$ are the leading order splitting functions which describe the probability of a parton p' with proton momentum fraction y radiating a parton with momentum $(1-\frac{x}{y})y$ leaving the interacting parton p (not necessarily the same species) with momentum fraction x. Figure 1.6 shows the Feynman vertices associated with each splitting function.

[‖]The fact that there are PDF contributions from gluons and anti-quarks will be explained in what follows.

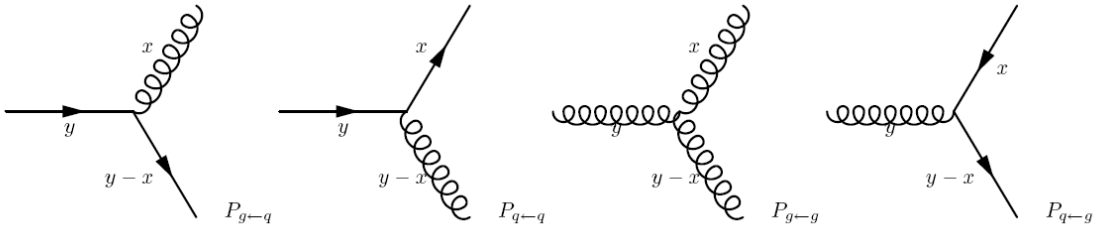

Figure 1.6: Feynman diagrams depicting parton splitting with corresponding splitting functions.

Figure 1.7[12] shows an example of a proton PDF for a value of $Q^2 = 10000\,\mathrm{GeV}^2$. Although the proton is said to be composed of the "valence" quarks uud it is clear that there are particles other than these valence quarks carrying some momentum fraction of the proton. The valence quarks dominate at high values of x. However, through $q\bar{q}$ loops all other types of quarks can be present as well; these are called "sea" quarks. Also, there is a very large contribution from the gluons at low x. The gluons make up a total of about 50% of proton's momentum, mostly at low x.

1.3.2 Perturbative QCD

As mentioned above, after factorizing the proton-proton interaction into three parts it is only the middle part, the hard parton-parton interaction which is calculable. This calculation is only possible because of the decreasing value of α_s with increasing characteristic momentum scale. The calculation of $\hat{\sigma}_{ab\to X}$ from equation 1.2 is done by means of a perturbative expansion in powers of α_s but is only valid for a $Q^2 \gg \Lambda^2$. Each term of the perturbative expansion includes Feynman diagrams with more vertices, which can result in internal loops or additional partons in the final state. Figure 1.8 shows an example of two higher order diagrams for the process $q\bar{q} \to q\bar{q}$.

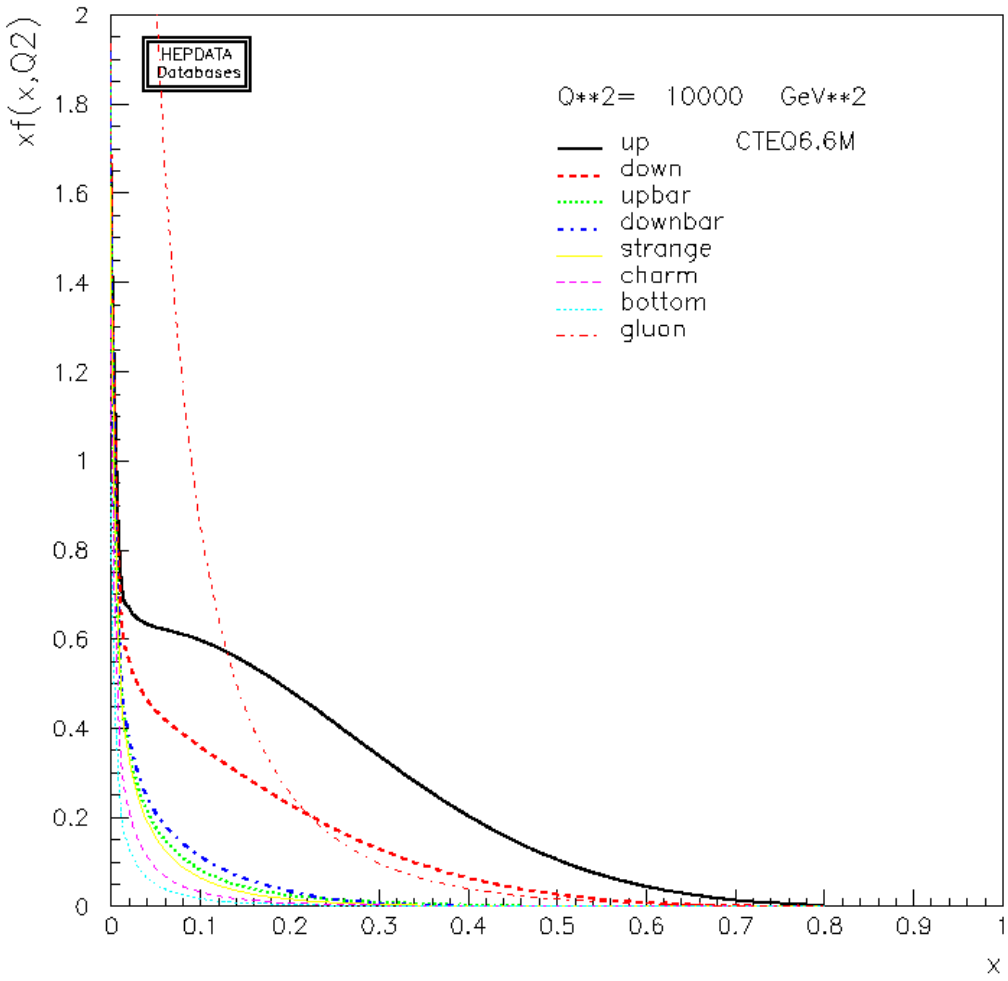

Figure 1.7: Proton PDFs at $Q^2 = 10000\,\mathrm{GeV}^2$.

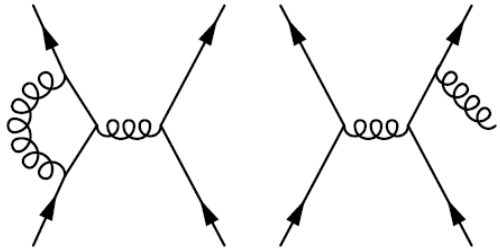

Figure 1.8: Examples of higher order $q\bar{q} \rightarrow q\bar{q}$ diagrams with internal (left) and final state (right) gluons.

The diagram with the final state gluon reflects the case in which the calculations to higher order correspond to a cross section for events with more than two jets. This concept of multiple parton topologies corresponding to higher order calculations will be important in later sections.

1.3.3 Fragmentation

After the perturbative calculation, to some order, is done to obtain $\hat{\sigma}_{ab\rightarrow X}$, the final step of the factorized problem is the long distance scale process that determines the fate of the outgoing partons. The probability of a parton radiating another parton at this point is $\mathcal{O}(\alpha_s \ln^2 \frac{Q^2}{\Lambda^2})$ and since $\alpha_s \sim \ln^{-1} \frac{Q^2}{\Lambda^2}$ there is a high probability that a parton is emitted. These emitted partons can in turn emit additional partons eventually resulting in a collection of partons, mostly travelling in the direction of the initial parton, which combine to form hadrons. This process is known as hadronization. The process of the partons radiating other partons and the subsequent hadronization together is called fragmentation.

Fragmentation, like the initial step of the factorized problem, is not calculable per-

turbatively but is treated in a similar manner to the parton density functions. The functions which describe the probability of evolution from a parton of type p to a hadron of type h, such that the hadron carries a fraction z of the parton's momentum, are called fragmentation functions $F_{h\leftarrow p}(z)$. Like PDFs these functions are determined from experiment and then applied to calculations universally. Also like PDFs, they evolve as a function of Q^2 so should be written $F_{h\leftarrow p}(z, Q^2)$.

1.4 Jets

The process of a proton-proton interaction, which was discussed in the previous section, results in groups of hadrons being formed travelling in approximately the same direction as the outgoing partons from the hard scatter. These collimated groups of hadrons are known as "jets". Although this is a nice picture of what happens to a single parton after some hard interaction, the picture is over-simplified. First of all, experimentally it is not possible to define a jet in this manner as there is no way to know if a final state particle came from a specific parton or not. Hence the definition of a jet needs to be formulated in a different way. A jet will therefore be defined as the result of a jet finding algorithm. Jet finding algorithms are tools which use the proximity of particles**, in either coordinate or momentum space, to group them together. These groups of particles are defined to be the jets. A jet algorithm also calculates the four momentum of the jet. This definition is also useful for theoretical calculations as the outgoing partons (and incoming ones for that matter) do not act

**The term particle is somewhat generic here. Really it can be any object with known four momentum. It will be shown that in experiment clusters of energy are used.

as independently as was described. Each coloured object in the event is influenced by many other coloured objects, so it may not be clear, even in calculation, how to match final state particles to partons (especially in light of the fact that fragmentation is a long distance phenomenon which is not calculable via perturbative QCD). Note that for a comparison between theory and experiment for a jet observable, it is necessary for the theorist and the experimentalist to implement the same jet algorithm. If an experimental result is a partonic measurement, that is, it is thought to describe the behaviour of the partons, not the particle jets, then this is not necessary. In the following the results are presented at the jet level. The details of the specific jet algorithm used are found in chapter 3.

1.5 Azimuthal Decorrelation

The focus of the analysis described in this thesis is a measurement of the azimuthal decorrelation in di-jet events resulting from proton-proton collisions in the LHC. The concept is to employ a simple observable that is sensitive to multi-jet production and robust against systematic effects.

As discussed above, knowing the protons' momenta does not uniquely dictate the momenta of the interacting partons. However, the partons inside the protons of the LHC beams have no appreciable momentum in the direction perpendicular to them therefore the vector sum of the total momentum in this direction must always be zero. It is conventional to define the plane perpendicular to the proton beam direction as the "transverse" plane. The component of a jet's momentum projected into this plane

is called the transverse momentum (p_T)[††]. The azimuthal decorrelation measurement is performed by measuring only the properties of the two leading jets ("leading" refers to the jets with the highest p_T). The advantage of this observable is that it can be used to test perturbative QCD predictions at orders higher than LO (since it is sensitive to multi-jet production) or can be compared to Monte Carlo simulations (that may only make calculations to LO) which attempt to describe proton-proton collisions. It is beneficial to be able to have such a measurement while only having to measure properties of the jets with the highest transverse momentum since these jets are least sensitive to experimental confounds. The azimuthal decorrelation is one such measurement which looks at the angle ($\Delta\phi$) in transverse plane between the two leading jets. Figure 1.9 shows the correspondence between jet multiplicity and $\Delta\phi$ range. Since the final vector sum of the p_T of all objects in an event must be zero, in the case where there are only two jets in an event, the requirement that the jets' p_T must balance forces $\Delta\phi = \pi$. As more jets are present in the events the possible range of $\Delta\phi$ includes values $< \pi$. The smaller the value of $\Delta\phi$ the more decorrelated the leading jets are said to be. More details regarding how this observable is defined and measured are found in chapter 5. A similar measurement has been reported by the D0 collaboration[13]. These results will be discussed briefly in chapter 6.

[††]Note that throughout this document the convention of expressing momenta in units of GeV is used as opposed to units of $\frac{GeV}{c}$.

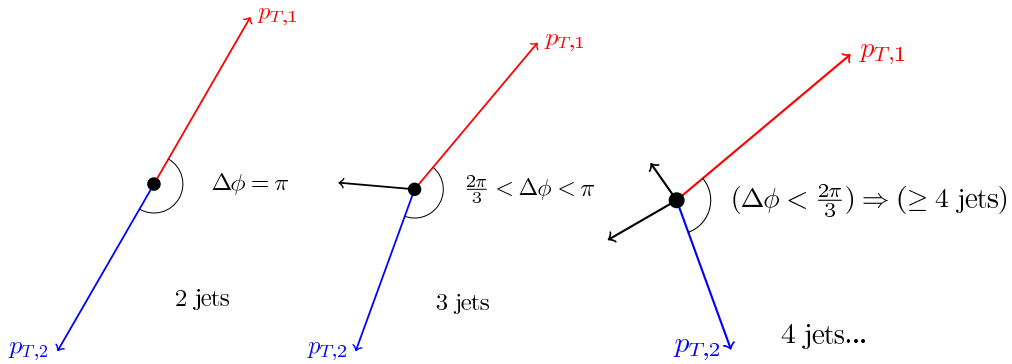

Figure 1.9: Correspondence between jet multiplicity and $\Delta\phi$.

Chapter 2

The ATLAS Detector and the LHC

The ATLAS detector [14, 15, 16] is one of the two general purpose detectors at the Large Hadron Collider (LHC)[17]. It has been designed to provide precision measurements of the energy, momentum and trajectory of particles resulting from the collision of protons at one of the LHC's four interaction points. This chapter will give an overview of the LHC and a description of the ATLAS detector, which will focus on the parts of the detector which are of relevance to this analysis. Unless otherwise stated, the figures in this chapter are taken from [14].

2.1 The Large Hadron Collider

The Large Hadron Collider at the European Organization for Nuclear Research (CERN), is a proton-proton collider located $\sim$ 100 m underground below Switzerland and France near Geneva, Switzerland. It occupies the 27 km long underground tunnel which was first built to house the Large Electron Positron Collider (LEP), which as the name implies, was an e^+e^- collider. LEP was just one in a series of colliders which have been built and (hopefully) will be built in the future. The predecessor to LEP at CERN, was the Super Proton Synchrotron (SPS). This accelerator began commissioning in 1976 and was in operation until the mid 1980's bringing protons and anti-protons into collisions at energies up to 400 GeV per beam. During this time the $W^{\pm}$ and Z^0 boson were discovered at the SPS[18][19] lending great credence to the SM. The SPS was later converted into an e^+e^- accelerator which was used as an injector for the LEP collider which began operation in 1989. Although there were no discoveries made at LEP it benefited from the relatively clean environment of a lepton collider and was able the make very high precision measurements[20] in the electroweak sector as well as putting mass limits on particles which have not (yet) been discovered. Independent of CERN, in Illinois, USA, a proton anti-proton collider (The Tevatron) was built and began operation in 1983 with beam energies of $\sim$ 900 GeV per beam. The last quark to found experimentally (the top quark) was discovered at the Tevatron in 1995[21]. None of the experiments at these colliders have been able to discover the Higgs boson, although all of the results are still consistent with its existence and the LEP experiments have been able to put a lower limit on its mass of 114 GeV[22]. It remains the only piece of the SM to be observed directly in experiment.

The search for the Higgs boson is one of the motivations for building the LHC, however not the only one. There are a host of theories beyond the Standard Model (BSM) which can explain some phenomena that are not addressed in the SM. Without going into detail, some examples are Super Symmetry (SUSY), Universal Extra Dimensions (UED) and theories which involve heavy versions of the vector bosons (W' and Z'). Each of these theories has regions of their parameter space which will be accessible at the LHC via the production of heavy particles which have never before been observed.

The LHC is poised to confirm or deny the existence of the Standard Model Higgs particle and to discover or limit the viability of BSM theories. In the tradition of hadron colliders making discoveries, and electron positron colliders making precision measurements, planning is underway for a future TeV-scale electron positron collider. If built this machine would allow for high precision measurement of the properties of any phenomena discovered at the LHC.

The LHC consists of ~ 1200 superconducting dipole magnets which are used to bend proton beams around its circumference. These magnets are cooled by superfluid liquid helium, are maintained at a temperature of 2 K and can achieve a magnetic field of 8 T. The LHC also includes ~ 400 superconducting quadrupole magnets used for beam focusing.

The LHC accelerator is the final machine in a chain of accelerators which together bring protons up to their collision energy. The accelerators leading up to the LHC are known as the injection chain. Figure 2.1 shows a schematic (not to scale) of the LHC and the injection chain. The injection chain consists of:

Linac2 A linear accelerator that accelerates the protons to an energy of 50 MeV.

Proton Synchrotron Booster (PSB) The first of three circular accelerators the PSB brings the protons up to 1.4 GeV.

Proton Synchrotron (PS) The PS, which started operation as a standalone accelerator in 1959, brings the protons from $1.4 \rightarrow 25$ GeV.

Super Proton Synchrotron (SPS) The SPS accelerator which began operation in 1976 was CERN's primary research machine through to the mid 1980's. It now serves as the final stage in the injection chain accelerating protons from $25 \rightarrow 450$ GeV and injecting them, via two transfer lines, into the LHC.

The protons injected into the LHC are grouped into bunches. Once injected, the proton bunches are accelerated by an RF system that operates at 400 MHz with a voltage per beam of $8 - 16$ MV. This accelerates the proton bunches to their final collision energy.

There are two important parameters when considering the physics reach of a particle collider: the centre of mass energy and the instantaneous luminosity. The centre of mass energy is the energy which is available in the colliding particles (protons in the case of the LHC) for production of other particles. Increasing the centre of mass energy can increase the cross section of a process of interest or provide enough energy to be above a production threshold for massive particles, such as the Higgs or particles from BSM theories. The instantaneous luminosity is related to the rate at which collisions take place. For rare processes, a high instantaneous luminosity is important in order to increase the probability of observation. Figure 2.2[23] shows

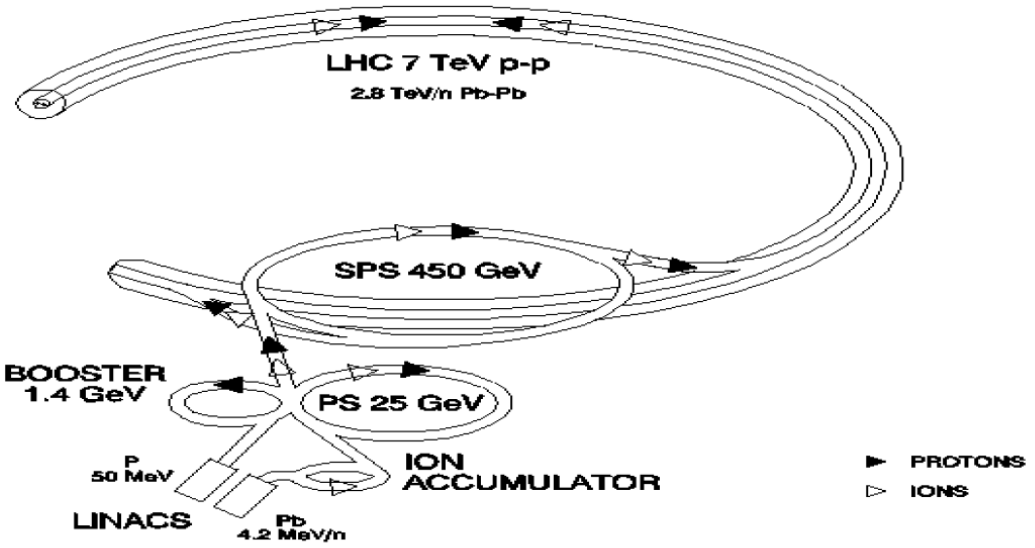

Figure 2.1: Schematic of the LHC and the injection chain. Not to scale.

the centre of mass energy ($\sqrt{s}$) and cross section (σ) for some processes at the LHC. The right-side y-axis shows the rate (in Hz) of events produced as a function of $\sqrt{s}$. The curves on the plot correspond to various physics processes of interest. The numbers given for the event rate are for the LHC maximum design luminosity and the event rate scales linearly with this number, i.e. the event rate is proportional to the instantaneous luminosity. Note that the event rate also increases (over this energy range) as $\sqrt{s}$ increases. This plot also shows the predicted cross sections for some BSM physics processes, for example, $\tilde{g}$ and $\tilde{q}$ refer to particles associated with SUSY.

The LHC has been designed to operate at a maximum centre of mass energy, $\sqrt{s}$, of 14 TeV with a maximum instantaneous luminosity of $\mathcal{L} = 10^{34}\,\mathrm{cm}^{-2}\mathrm{s}^{-1}$. A discussion of luminosity can be found in chapter 4. This luminosity is achievable by filling

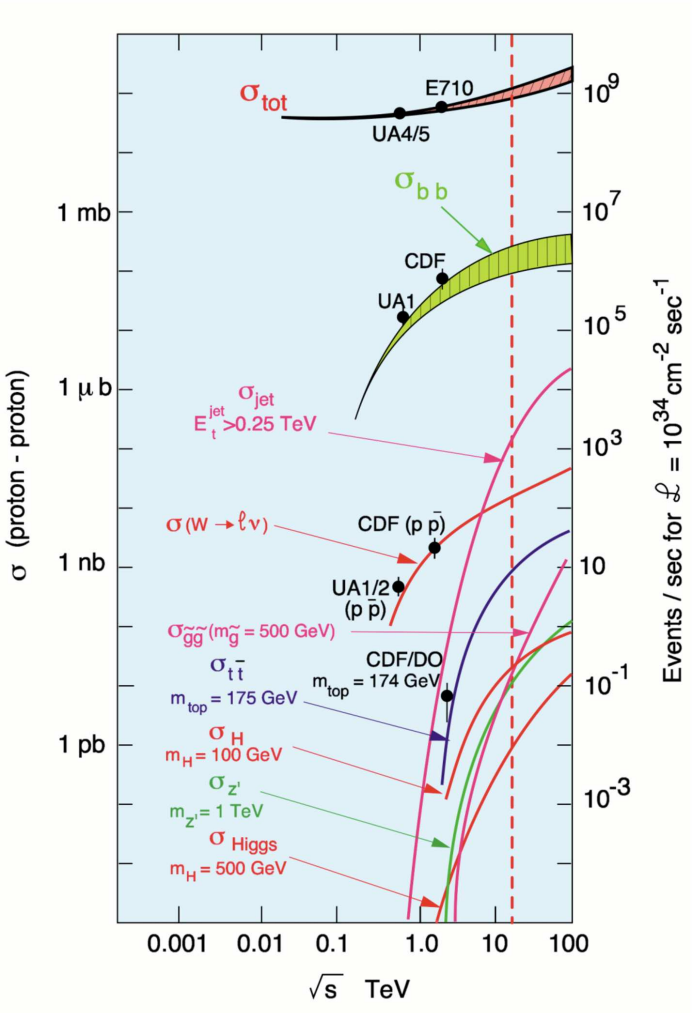

Figure 2.2: Production cross sections and rates as a function of $\sqrt{s}$ for some standard model and beyond the standard model processes.

the LHC with ~ 2800 bunches each containing $\sim 10^{11}$ protons. During the period that the data for the analysis in this thesis were taken, the LHC was operating at $\sqrt{s} = 7\,\text{TeV}$ (half of the design energy), and achieving instantaneous luminosities of $\mathcal{L} \sim 10^{29} - 10^{30}\,\text{cm}^{-2}\text{s}^{-1}$, with 16 or fewer bunches in the machine with $10^{10} - 10^{11}$ protons per bunch. With this few protons per bunch the probability of have multiple proton-proton interactions is small. With more protons per bunch up to 20 interactions per bunch crossing are expected. This phenomenon is known as "pileup" and can affect the measured energy of objects in the detector. However, this is not of concern in the data set considered for this analysis.

In 2008 the LHC started the magnet commissioning process to prepare for beam energies of 7 TeV per beam. During this process one of the magnets experienced an electrical short which resulted in a breech in the magnet's cryostat, explosively venting many tonnes of helium and damaging many magnets. This took approximately one year to repair. Although this type of problem which caused the accident can now be foreseen and avoided, the current, lower than nominal, conditions for the LHC energy and luminosity are precautions. This said, the LHC initial performance is still very encouraging, as it is the highest energy hadron collider in the world. The collider to previously hold the record is the Tevatron $p\bar{p}$ collider in the United States which operates at $\sqrt{s} \sim 2\,\text{TeV}$ and $\mathcal{L} \sim (10^{32} - 10^{33})\,\text{cm}^{-2}\text{s}^{-1}$.

2.2 The ATLAS Detector

ATLAS is composed of three main detector subsystems, which are shown in figure 2.3:

- **Muon Spectrometer** which consists of the muon chambers and superconducting toroidal magnets.
- **Inner Detector** which consists of the silicon detector, the semiconductor tracker, the transition radiation tracker and the solenoid magnet.
- **Calorimeter** which consists of the liquid argon (LAr) electromagnetic calorimeter, the tile calorimeter and the forward hadronic calorimeters.

These detector systems are generally divided into a "barrel" region corresponding to the central part of the detector, and "endcap" regions corresponding the the forward parts of the detector. The sub-systems of the inner detector which extend into the endcap use the same technology as is used in the barrel region. The muon system and calorimeter systems however, use different technologies in the endcap and barrel regions in some instances. The analysis that follows focuses on jets reconstructed in the central region of the calorimeter and thus the barrel is given more emphasis.

The detector also relies on a trigger system which dictates which data events are recorded.

The detector subsystems and the trigger are described in more detail in the following sections, following a discussion of the coordinate system defined for ATLAS. Note that neither the muon spectrometer nor the inner detector are of significant importance* to the following analysis. For this reason the description of these components of the ATLAS detector are is somewhat brief, while the description of the calorimeter is more in depth.

*Although a vertex reconstructed by the inner detector is required.

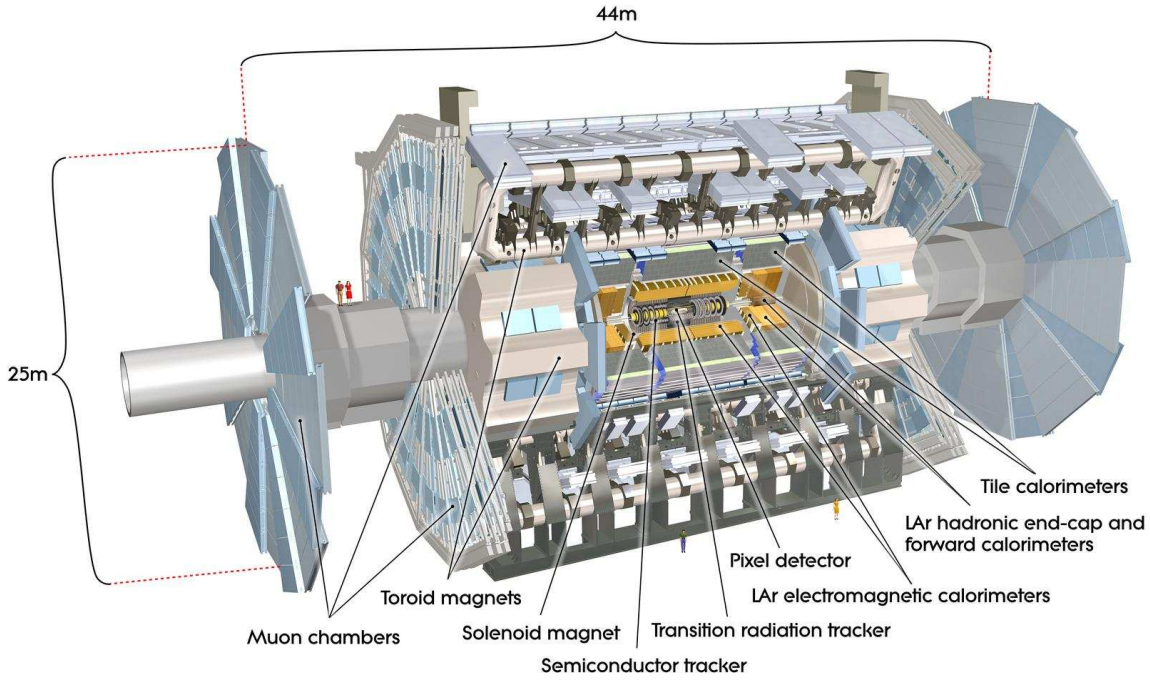

Figure 2.3: The ATLAS Detector

2.2.1 Coordinate Systems

There are three ATLAS coordinate systems to consider. They are:

1. A right handed Cartesian coordinate system (pictured in figure 2.4) centred at the interaction point, in which the y-axis is straight up, the x-axis points toward the centre of the LHC, and the z-axis points along the beam direction.

2. A spherical coordinate system based on the Cartesian system, using the azimuthal angle ϕ, which is the angle measured in the x-y plane up from the x-axis, θ, the polar angle measured up from the z-axis and s the distance to the origin.

3. A cylindrical coordinate system based on the Cartesian system, using the same azimuthal angle ϕ as above, the perpendicular distance to the z-axis (R) and the z coordinate.

Note that in the following, the angle θ is not used but rather the coordinates rapidity, y, and pseudo-rapidity, η. For the description of jet direction in a physics measurement the quantity y is used where

$$y = \frac{1}{2} \ln \left(\frac{E + p_z}{E - p_z} \right) \ . \tag{2.1}$$

Here E is the energy and p_z is the projection of the momentum in the z-direction. In some cases, it is more convenient to use pseudo-rapidity η which is $\lim_{m \to 0} y$, where m is mass, or

$$\eta = \frac{1}{2} \ln \left(\frac{|\vec{p}| + p_z}{|\vec{p}| - p_z} \right) \tag{2.2}$$

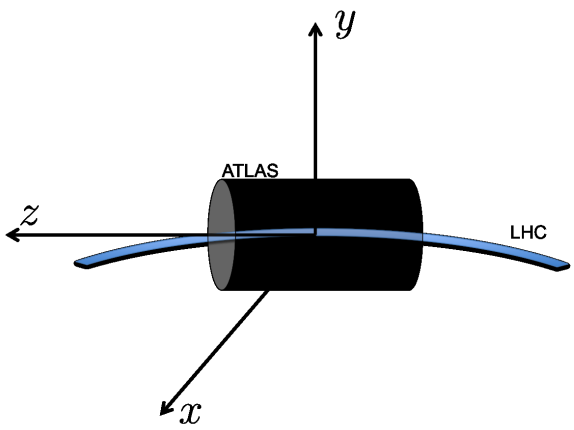

Figure 2.4: The ATLAS coordinate system.

which reduces to

$$\eta = -\ln\left[\tan\left(\frac{\theta}{2}\right)\right] . \tag{2.3}$$

This quantity is independent of particle mass and depends only on the angle θ making it more suitable for referring to quantities related to the detector itself, for example coverage or location of detector components.

2.2.2 Muon Spectrometer

The muon spectrometer, depicted in figure 2.5, is designed to accurately measure the momenta of muons which are expected to pass through and exit the detector. The muon spectrometer can record space point hits up to $|\eta| < 2.7$. This system is the outermost detector and relies on a magnetic field in the circumferential direction which is generated by the toroidal magnets. Charged muons' trajectories are bent in this magnetic field and space point measurements are made using precision tracking chambers in order to reconstruct the muons' trajectories to calculate the momentum.

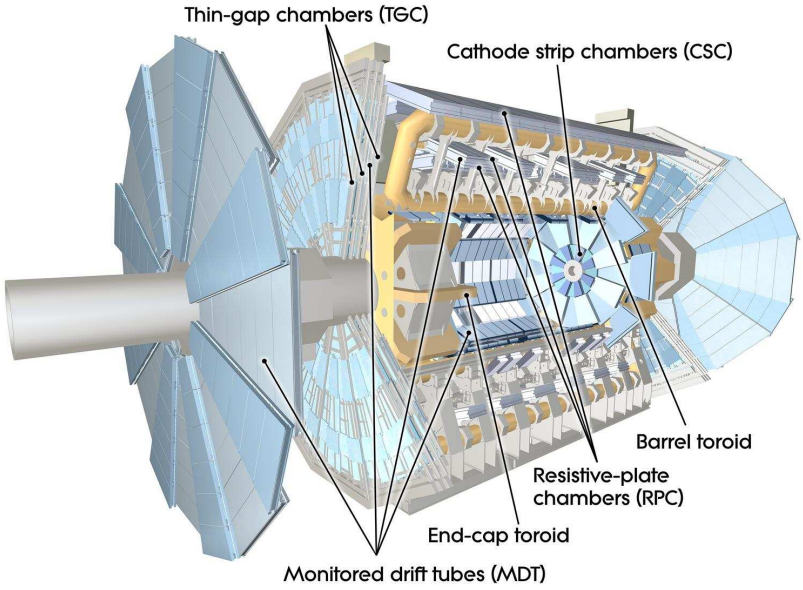

Figure 2.5: The ATLAS Muon Spectrometer

These chambers are known as the monitored drift tubes (MDTs). Planes of MDTs are arranged in layers of 3 or 4 at three sampling distances in the barrel region, inner ($R \approx 4.5 - 6\,\mathrm{m}$), middle ($R \approx 7 - 8\,\mathrm{m}$) and outer ($R \approx 9 - 11\,\mathrm{m}$). The muon spectrometer is designed to have a standalone momentum resolution of 10% for 1 TeV muons. The central region of the muon system also includes modules with resistive plate chambers (RPCs) in order to deliver track information within a few tens of nano seconds for the purpose of muon triggering up to $|\eta| = 2.4$. In the forward region the particle flux is too high for the MDTs and they are replaced with cathode strip chambers (CSCs) which can be operated with a higher hit occupancy. The forward boundary of the muon system is at $|\eta| = 2.7$. The muon endcap trigger information comes from the thin gap chambers (TGCs) which are located behind the endcap calorimeters.

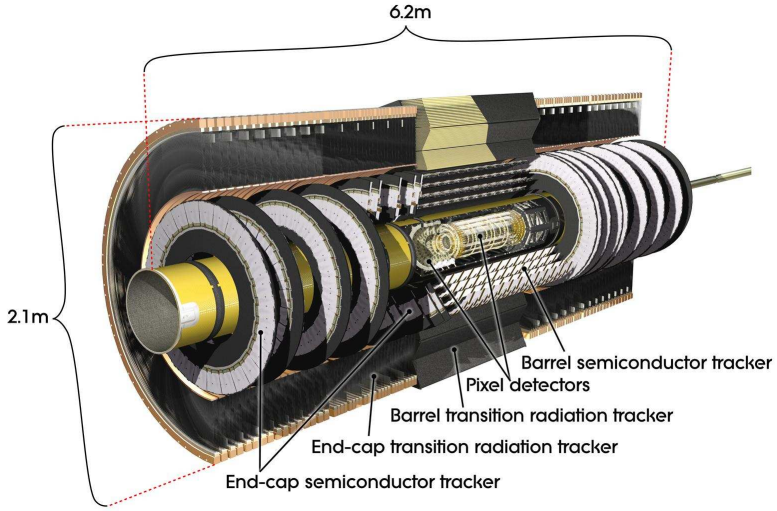

Figure 2.6: ATLAS Inner Detector showing the SCT the pixel and TRT detectors.

2.2.3 Inner Detector

The inner detector (ID), depicted in figure 2.6, consists of three independent subsystems; the silicon pixel detector, the silicon microstrip (SCT), and the transistion radiation tracker (TRT), all of which are located inside a $2\,T$ solenoid magnet. Figure 2.7 shows the distances to the beam axis of the ID subsystems. The ID is designed to reconstruct the paths of charged particles passing through it both for the reconstruction of vertices and to make momentum measurements. The pixel detector and SCT use finely segmented solid state silicon components in order to give high precision spatial measurements while remaining radiation hard. The pixel detector consists of $\approx 8 \times 10^7$ pixels of nominal size $50 \times 400\,\mu\text{m}^2$ and provides single space point hit resolution of $10\,\mu$m and $115\,\mu$m in the $R-\phi$ and the z directions respectively. The SCT consists of $\approx 6 \times 10^6$ channels with a strip pitch of $80\,\mu$m and is designed to provide a spatial resolution of $17\,\mu$m and $580\,\mu$m in the $R-\phi$ and the z directions respectively. The SCT consists of a barrel section which provides hit information in

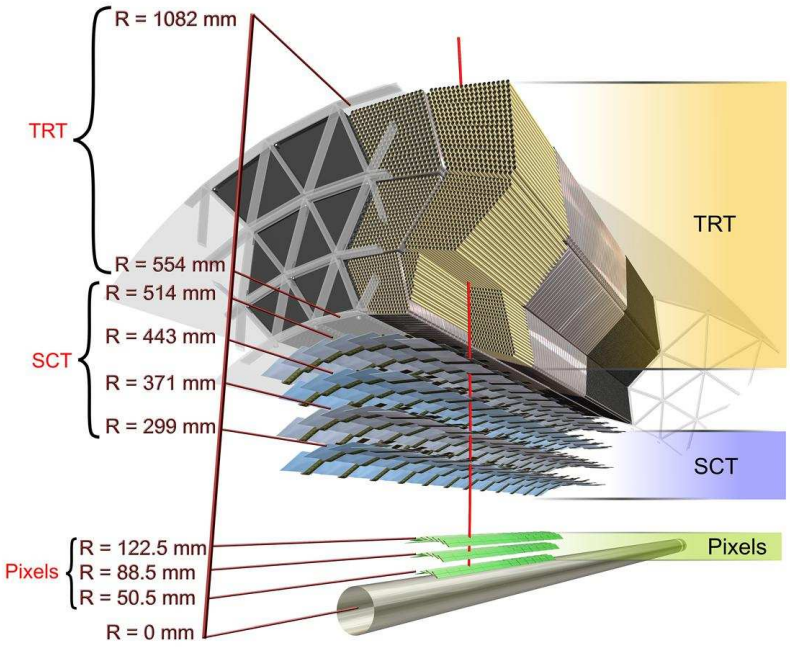

Figure 2.7: Exploded view of the ATLAS Inner Detector showing the R positions of the components.

the range of $|\eta| < 1.6$ and an endcap section which extends to $|\eta| \sim 2.5$. The TRT consists of $\approx 4 \times 10^5$ drift tubes (or "straw tubes") of diameter 4 mm which provide measurements in $R - \phi$ in the barrel and in z$-\phi$ in the endcap improving the momentum resolution of the ID with a single straw tube position resolution of 130 μm. The TRT consists of a barrel section which extends to $|\eta| \sim 1$ and an endcap section which extends to $|\eta| \sim 2.2$.

2.2.4 Calorimeters

Sampling Calorimeters

All of the calorimeter sub-systems of the ATLAS detector are sampling calorimeters. These devices are designed to measure the energy of incident particles by means of alternating layers of absorber and active materials. The absorber material, is typically much more dense than the active material. Incident particles undergo cascades of interactions resulting in showers of particles. Through the shower the incoming particle loses all of its energy to these showered particles which deposit all of their energy into the calorimeter. A sampling calorimeter is designed to measure the energy of the incident particle using the energy deposited in the active regions by ionization.

Showers are caused by repeating interactions in which a single particle branches into multiple particles which in turn branch into multiple particles resulting in more and more particles with decreasing average energy as the shower proceeds. Depending on whether or not the incident particle is a hadron or an electromagnetic particle

(electron[†] or photon) the shower development is different.

Electromagnetic showers are initiated by high energy electrons or photons and consist of electrons and photons. These particles are produced in a series of Bremsstrahlung and e^+e^- pair production processes until the showered particles' energies are sufficiently low for the probabilities of Compton scattering and the photoelectric effect to be dominant. Most of the energy of these showers is deposited in the absorber and a small amount is deposited in the active medium. The fraction of the energy of an electromagnetic shower which is deposited in the active regions is called the electromagnetic sampling fraction. The sampling fraction is used to convert from the measured energy to the total energy of the electromagnetic shower.

Hadrons incident on the calorimeter produce hadronic showers which are the result of a series of inelastic hadron-nucleon interactions and consist of mostly $\pi^{\pm}$ and π^0 particles. The π^0's decay almost immediately into photons which shower electromagnetically, which means that hadronic showers contain electromagnetic showers within them. The electromagnetic showers are more compact resulting in an EM core within the shower. The charged pions continue to interact producing more and more particles. The energy of a hadronic shower is sampled in the same way as an electromagnetic shower however there is an additional complication. The strong interactions of the hadrons and nucleons can result in particles losing energy to nuclear excitations, neutrino or muon production through hadron decay, nuclear break-up or slow neutrons; processes that do not result in ionization in the active medium. This is referred to as invisible energy. The energy of a hadronic shower measured by the calorimeter is said to be at the electromagnetic scale ("em-scale") and does not rep-

[†]In this section "electron" refers to electrons or positrons.

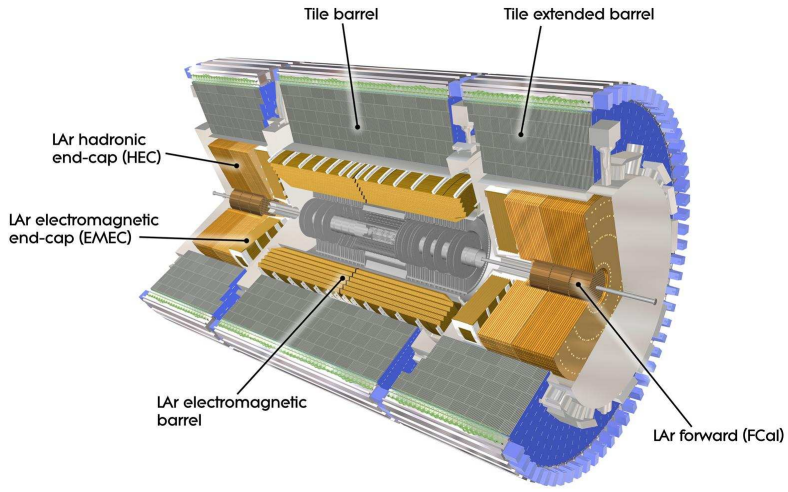

Figure 2.8: The ATLAS Calorimeters

resent the energy of the incident hadron. The ratio between the actual value and the measured value is called $\frac{e}{h}$ and is > 1. A calibration to account for this effect needs to be applied. Details of this procedure can be found in chapter 3.

The ATLAS Calorimeters

The ATLAS calorimeter, depicted in figure 2.8, consists of five subsystems: the tile calorimeter, the hadronic endcap calorimeter (HEC) and the forward calorimeter (FCal), which compose the hadronic calorimetry system, and the electromagnetic barrel (EMB) and electromagnetic endcap (EMEC) calorimeters which make up the electromagnetic calorimetry system. There are three cryostats in the ATLAS detector. The EMB is contained in the barrel cryostat and EMEC, HEC and FCal are all contained in two endcap cryostats (one at each end of the detector).

The ATLAS calorimeter system was designed to measure particle energies uniformly

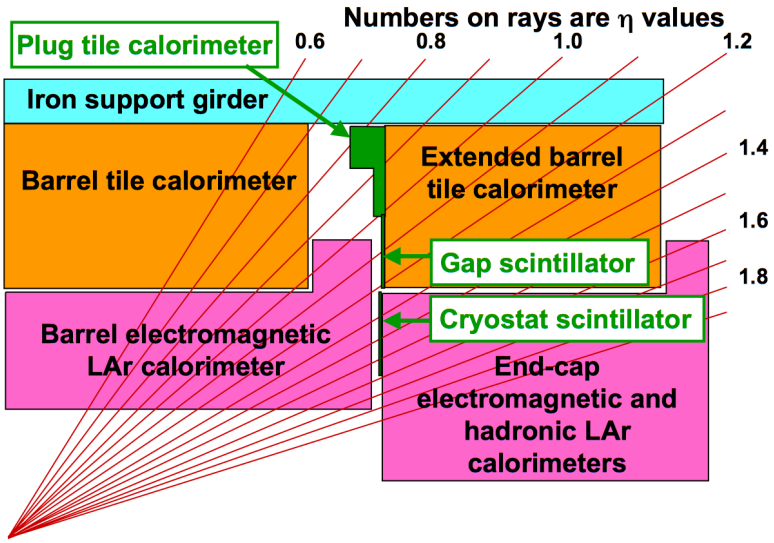

Figure 2.9: Schematic of the calorimeter cut away in the $R - z$ plane showing the boundaries in pseudo-rapidity. Note that the FCal is not included.

over the full range in azimuth and up to a pseudo-rapidity of ≈ 5. Figure 2.9 shows a schematic of the calorimeter cut away in the $R - z$ plane showing the boundaries in pseudo-rapidity for all the calorimeter systems with the exception of the FCal.

The readout of each calorimeter is segmented in depth (longitudinally) and in η and ϕ. Each segment is referred to as a "cell". The cell includes the active and absorber regions within its boundary. The cells' geometry is projective back to the interaction point. The segmentation granularity varies for each subsystem and within each subsystem. The active regions of each cell are instrumented together and there is a unique electronics channel associated with each cell. Cell granularities are listed in the sections that follow.

The Electromagnetic Calorimeter

The electromagnetic (EM) calorimeter is made up of the EMB and EMEC. The details of their pseudo-rapidity ranges, longitudinal segmentation and cell granularity are listed in table 2.1[15]. Note that the granularity of each sampling layer decreases with depth. The very fine segmentation of the first sampling layer improves the calorimeter's position resolution. The majority of the energy of an electromagnetic shower is deposited in the second sampling layer. The granularities of the layers affect the jet p_T and position resolutions, which are discussed in chapter 5. Both of these subsystems are sampling calorimeters that use lead as the absorber material and liquid argon as the active medium. The active and absorber layers are said to have an accordion geometry which is illustrated for a section of the EMB in figure 2.10. The EMEC accordion geometry differs slightly. This geometry allows for complete coverage (without gaps) in the azimuthal direction.

Before assembly of the calorimeter a section of the EMB calorimeter was tested by means of an electron test beam and the single particle resolution and response linearity were measured. The linearity and the fractional energy resolution ($\frac{\sigma_E}{E}$), are shown in figure 2.11[14]. The fractional resolution is conventionally parameterized as:

$$\frac{\sigma_E}{E} = \frac{a_1}{\sqrt{E}} \oplus a_2 \oplus \frac{a_3}{E} \ . \tag{2.4}$$

The three parameters a_1, a_2 and a_3 of this parameterization describe what are known as the sampling term, the constant term and the noise noise term, respectively. The sampling term (sometimes called the stochastic term) is due to statistical fluctuations which have a variance proportional to n where n is the number of charged particles

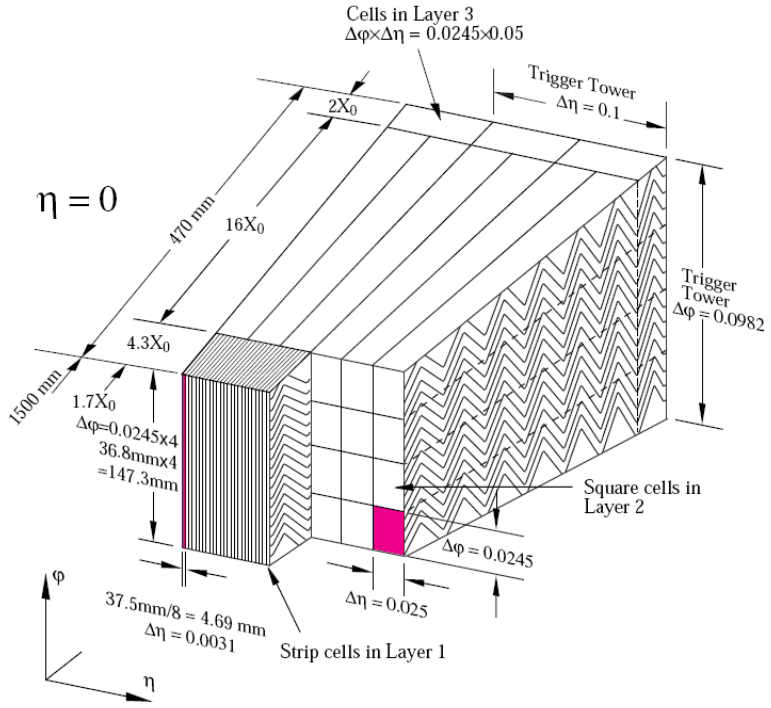

Figure 2.10: Diagram of a section of the ATLAS electromagnetic barrel calorimeter. The accordion geometry and the segmentation in azimuth and pseudo-rapidity are shown.

from a shower passing through the active region. The energy E is proportional to n making the relative energy resolution due to statistical fluctuations proportional to $E^{-\frac{1}{2}}$. The constant term is due to resolution effects which are proportional to the energy, making the fractional resolution independent of energy. Examples of such effects are: gaps in the detector coverage[‡], detector non-uniformities or calibration problems. The noise term describes the contribution to the energy resolution due to effects, such as electronics noise, which are independent of the energy making an effect on the fractional energy resolution $\propto E^{-1}$.

[‡]The desire for good detector coverage and hence a lower constant term was one of the reasons for the EM calorimeters' accordion geometry.

Table 2.1: Pseudo-rapdity, longitudinal segmentation and granularity of the electromagnetic calorimeter.

EM Calorimeter	Barrel	End-cap	
Coverage	$\|\eta\| < 1.475$	$1.375 < \|\eta\| < 3.2$	
Longitudinal segmentation	3 samplings	3 samplings	$1.5 < \|\eta\| < 2.5$
		2 samplings	$2.5 < \|\eta\| < 3.2$
Granularity ($\Delta\eta \times \Delta\phi$)			
Sampling 1	0.003×0.1	0.025×0.1	$1.375 < \|\eta\| < 1.5$
		0.003×0.1	$1.5 < \|\eta\| < 1.8$
		0.004×0.1	$1.8 < \|\eta\| < 2.0$
		0.006×0.1	$2.0 < \|\eta\| < 2.5$
		0.1×0.1	$2.5 < \|\eta\| < 3.2$
Sampling 2	0.025×0.025	0.025×0.025	$1.375 < \|\eta\| < 2.5$
		0.1×0.1	$2.5 < \|\eta\| < 3.5$
Sampling 3	0.05×0.025	0.05×0.025	$1.5 < \|\eta\| < 2.5$

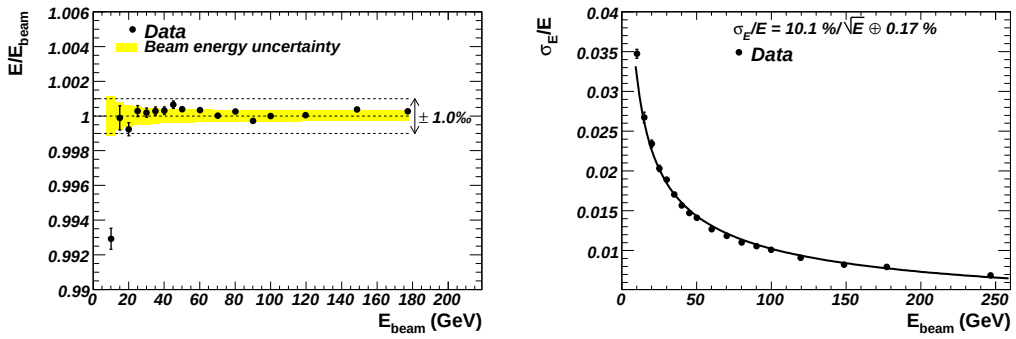

Figure 2.11: Linearity and single particle fractional energy resolution in the EMB as measured with an electron test beam ($\eta = 0.687$).

Table 2.2: Pseudo-rapdity, longitudinal segmentation and granularity of the hadronic end-cap calorimeter.

Hadronic LAr		
Coverage	$1.5 < \|\eta\| < 3.2$	
Longitudinal segmentation	4 samplings	
Granularity ($\Delta\eta \times \Delta\phi$)	0.1×0.1	$1.5 < \|\eta\| < 2.5$
	0.2×0.2	$2.5 < \|\eta\| < 3.2$

Table 2.3: Pseudo-rapdity, longitudinal segmentation and granularity of the forward calorimeter.

Forward Calorimeter	
Coverage	$3.1 < \|\eta\| < 4.9$
Longitudinal segmentation	3 samplings
Granularity ($\Delta\eta \times \Delta\phi$)	$\sim 0.2 \times 0.2$

The Hadronic Calorimeter

The hadronic calorimeter is composed of the HEC, the FCal and the tile calorimeters. The HEC and FCal are, like the EM calorimeter, sampling calorimeters which use liquid argon as the active medium. The HEC uses copper as the absorber material and the FCal, which has three sampling layers, has a copper sampling layer followed by two tungsten sampling layers. The coverage, granularity and longitudinal segmentation are detailed in tables 2.2 and 2.3[15].

The tile calorimeter is a sampling calorimeter consisting of alternating layers, in the z-direction, of steel and scintillator (which is the active medium). The scintillator-steel layers are constructed into 64 wedge shaped modules that form a self supporting structure. A diagram of one of the modules showing the orientation of the steel and scintillators is shown in figure 2.12. The scintillators are connected to wavelength shifting fibres which transmit the light signal from the scintillators to photo multiplier tubes (PMTs). The specifications regarding the tile calorimeter's coverage,

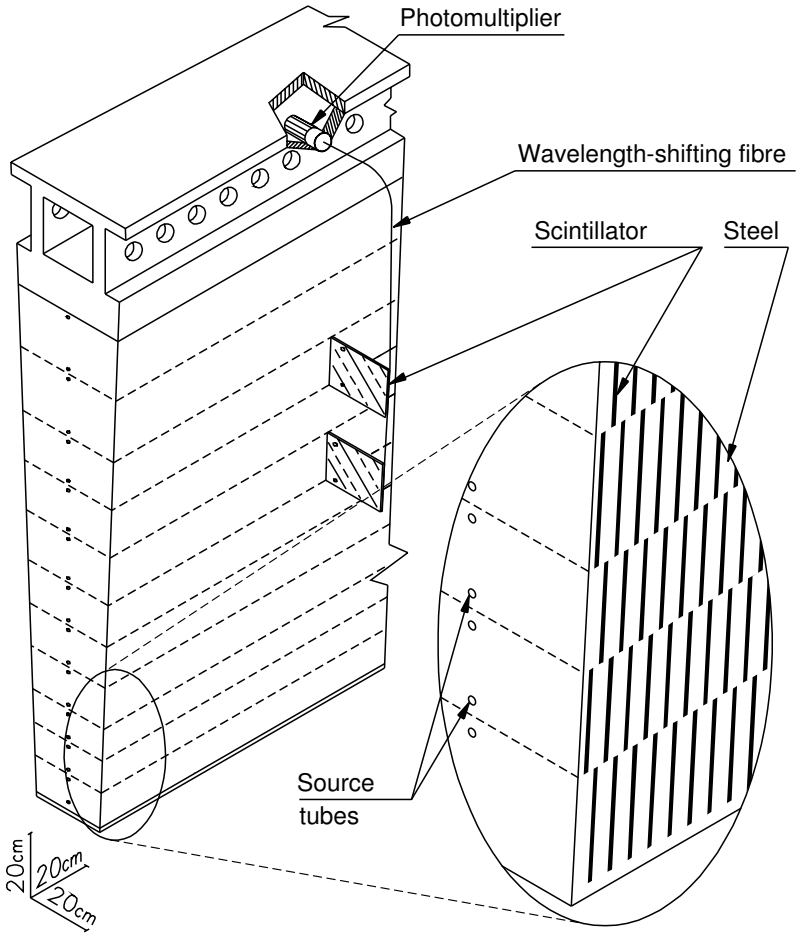

Figure 2.12: Diagram of one of 64 tile wedge modules.

segmentation and granularity are shown in table 2.4[15].

To measure the single particle response using the tile and LAr calorimeters, part of the EM calorimeter and tile calorimeter were tested simultaneously (in the same relative configuration as in the ATLAS detector) using pion beams of known energy. From this, the combined response linearity and fractional energy resolution for single pions were measured and can be seen in figure 2.13[14] along with a fit to a parameterization of the fractional resolution.

Table 2.4: Pseudo-rapdity, longitudinal segmentation and granularity of the hadronic tile calorimeter.

Hadronic Tile	Barrel	Extended Barrel
Coverage	$\|\eta\| < 1.0$	$0.8 < \|\eta\| < 1.7$
Longitudinal segmentation	3 samplings	3 samplings
Granularity ($\Delta\eta \times \Delta\phi$)		
Samplings 1 and 2	0.1×0.1	0.1×0.1
Sampling 3	0.2×0.1	0.2×0.1

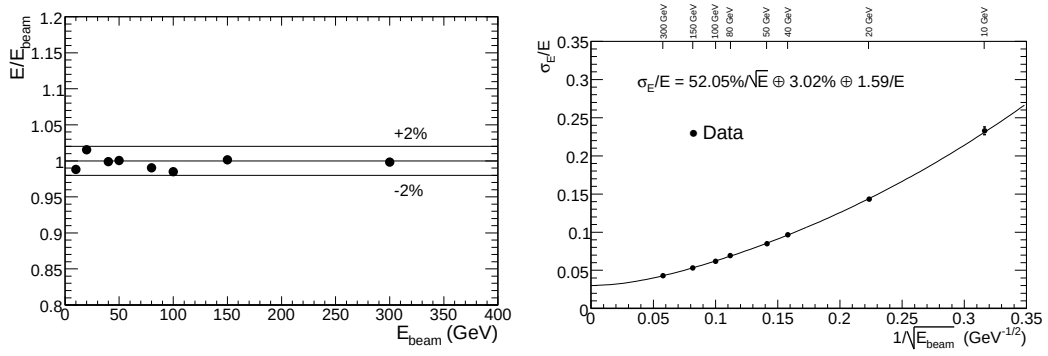

Figure 2.13: Linearity and single particle fractional energy resolution of the combined EMB and tile calorimeters as measured using a pion test beam ($\eta = 0.25$).

Calorimeter Signal Reconstruction

The goal of the signal reconstruction is to obtain a value for the energy deposited in a cell and to obtain timing information (relative to the LHC collision time for that event) for that cell. The energy and timing information are inputs into the reconstruction of physics objects from the calorimeter.

An ionizing particle passing through the active region induces a current pulse in the electronics. In the tile calorimeter this pulse is the output from a photomultiplier tube. In the liquid argon detectors the current pulse is a triangular signal, generated within the cell, which is amplified and shaped by the front-end electronics. An example of this shaped pulse and a triangular ionization pulse in the liquid argon electronics are shown in figure 2.14. Note that the area of the shaped pulse above zero (or pedestal) is equal to the area below zero. This ensures that many overlaid pulses, spread out over time sum to zero and do not shift the pedestal value. The shaped pulse is sampled each 25 ns and the samples are used to reconstruct the cell energy (E) and timing (τ) for that cell. These values are reconstructed by applying optimal filtering coefficients (OFCs) to the n samples around the peak of the pulse. The OFCs are two sets of values a_i and b_i which are applied to the sample values such that

$$E = \sum_{i}^{n} a_i \cdot s_i \tag{2.5}$$

and

$$E\tau = \sum_{i}^{n} b_i \cdot s_i \tag{2.6}$$

where s_i are the sample amplitudes in ADC counts. A simplified χ^2 parameter is also

calculated to quantify the agreement between the measured signal and the expected signal. It is defined as

$$\chi^2 = \sum_i^n (s_i - E(g_i - \tau \frac{dg_i}{dt}))^2 \tag{2.7}$$

where g_i is the normalized pulse shape expected from a particle passing through the active medium. The value of χ^2 can be used to determine if a signal is from a particle passing through the active region or from electronics noise.

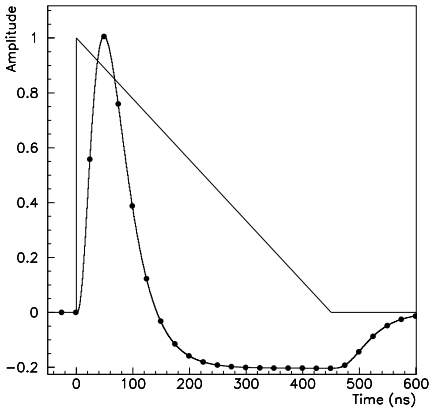

Figure 2.14: Example of a liquid argon electronics pulse shape, showing 25 ns sampling, resulting from the overlaid triangular ionization pulse.

Electronics Calibration

The liquid argon and tile calorimeters both have precision charge-injection systems which are used to calibrate the electronics response. These systems are used to inject a current pulse into the readout electronics. In the tile calorimeter the pulse is injected in the electronics after the PMTs and emulates the shape of the PMT

signal. In the LAr calorimeters it is injected onto the calorimeter electrodes[§]. The LAr injected pulse shape is designed to mimic the current pulse expected due to an ionizing particle passing through the active medium. The amplitude and time relative to the sampling time of the electronics can be adjusted in these calibration pulses. Three types of dedicated calibration runs are taken. These are, ramp runs, delay runs and pedestal runs. During a ramp run the calibration pulse amplitude is increased in steps throughout the run. From the data taken in these runs the output signal amplitude can be obtained as a function of the input pulse amplitude. During a delay run the pulse amplitude is held constant while a time delay is added between the input pulse injection time and the sampling time. This delay is shifted in 1 ns increments. The data from the delay runs allow for the reconstruction of the pulse shape with 1 ns time granularity, as opposed to the 25 ns sampling granularity. A pedestal run is a run in which the calorimeter is read out with no pulse being injected into the electronics. The mean value of the output from the electronics during one of these runs is known as the pedestal value, i.e. the average value expected with no signal pulse. The RMS of the values about this mean is defined as the characteristic noise in that channel. The data from the pedestal runs is also used to extract a matrix describing any correlations between the samples (known as the auto-correlation matrix).

The high time-granularity pulse shape, the pedestal value and the auto-correlation matrix are all used to calculate the OFCs described in the previous section. The ratio of the input to output amplitudes is used to obtain the overall normalization. The characteristic noise for each channel in stored in a database and is accessible for reconstruction and analysis, for example, to define a signal to noise ratio.

[§]The is true for all LAr calorimeter subsystems with the exception of the FCal, in which the pulse is injected into the electronics.

The tile calorimeter has two additional calibration systems, a laser system and ^{137}Cs source which is moved hydraulically through the detector, which are used to calibrate the light response of the scintillators and photomultipliers as a function of time. The laser system uses a 532 nm laser to inject pulses into the photomultipliers in dedicated runs and the response as a function of the pulse intensity is measured. The ^{137}Cs source is moved through the calorimeter, also in dedicated runs, and the response to the electrons from the beta decays of ^{137}Cs is measured and any changes over time can be accounted for.

2.2.5 Trigger

Main Trigger Chain

The LHC has the ability to collide bunches of protons at a rate of 40 MHz. It is not possible to write event data to disk at a rate that high, nor are all of the events of equal interest, so, as is the case for all collider experiments, a sophisticated trigger system is used at ATLAS. This trigger system operates at three levels, level-1 (L1), level-2 (L2) and event filter (EF). Each successive level uses the information from the previous level and then makes additional decisions. L1 reduces the event rate to ~ 75 kHz, L2 further reduces it to ~ 3.5 kHz and finally the event filter reduces the rate to ~ 200 Hz which is sufficient to be able to read out and record the data. Each level of the trigger has different "trigger items" that correspond to physics objects such as jets, electrons, photons or muons above some E_T threshold. For example the L2_EM30 trigger would be a level-2 trigger designed to trigger on electromagnetic objects (e or γ) with $E_T > 30$ GeV.

The L1 uses information from the muon system and the calorimeters to search for objects (e,γ, τ, μ and jets) with transverse momentum above a predefined threshold. To allow for a sufficiently short processing time this trigger level relies on field programmable gate arrays (FPGAs) which operate much more quickly than computation by computer processor. L1 provides a decision for each L1 trigger item individually and also supplies an associated region of interest (RoI) which specifies the region in the detector which will be read out and analyzed by the L2 trigger. The RoI is also of use in offline studies of the L1 trigger as it is the only available geometrical information associated with the L1 trigger decision.

The L2 trigger uses all of the detector information from the RoI supplied by L1, which typically represents $\sim 2\%$ of the total event. Physics objects (for example electrons or jets) are reconstructed at this stage and a decision for each trigger item is passed to the EF.

The EF runs reconstruction algorithms on a computer farm located on the surface above the ATLAS detector. These algorithms are very similar to those run offline after the data have been recorded. The EF has access to all the event data in memory and once physics objects have been reconstructed decisions can be made for each EF trigger item.

The L1 trigger system was the only trigger used during the early running period over which the data used here were recorded. The analysis described in this thesis uses only a level-1 jet trigger; the details of which are given in the following.

Level-1 Jet Trigger

The calorimeter jet trigger uses trigger towers as input. Each trigger tower is a grouping of all the cells in a predetermined area of 0.1×0.1 in $\Delta\eta \times \Delta\phi$ projected through all sampling layers of the electromagnetic and hadronic calorimeters. However, the L1 jet trigger algorithm uses objects of coarser granularity, "jet elements", which are the sum of 2×2 trigger towers resulting in a granularity of 0.2×0.2 in $\Delta\eta \times \Delta\phi$. From the jet elements two objects are constructed for use in the algorithm, a RoI which corresponds to 2×2 jet elements (0.4×0.4 in $\Delta\eta \times \Delta\phi$) and a jet window which is either 2×2, 3×3 or 4×4 jet elements. Each jet trigger item has a predefined jet window size. For each possible RoI the jet window is constructed as shown in figure 2.15. This figure shows that the 2×2 and 4×4 windows only have one possible configuration, while the 3×3 window has four possible configuations. For each possible RoI the sum of the E_T of all the towers in the jet window is calculated (for 3×3, the window with the highest E_T configuration is used). The algorithm is satisfied if both of two conditions are met. The first condition is that the sum of E_T in the jet window is greater than some specified value which is fixed for that trigger item. The second condition is that the RoI is a local maximum. That is considered to be the case if the sum of its E_T is greater than that of all its neighbours on two connected sides and greater than or equal to that of its neighbours on the opposite sides, as shown in figure 2.16.

In the analysis which follows, the jet trigger used is the L1_J5 trigger. This trigger requires the sum of the E_T in the jet window to be $\geq 5\,\text{GeV}$ and uses a jet window of size 0.8×0.8 in $\Delta\eta \times \Delta\phi$.

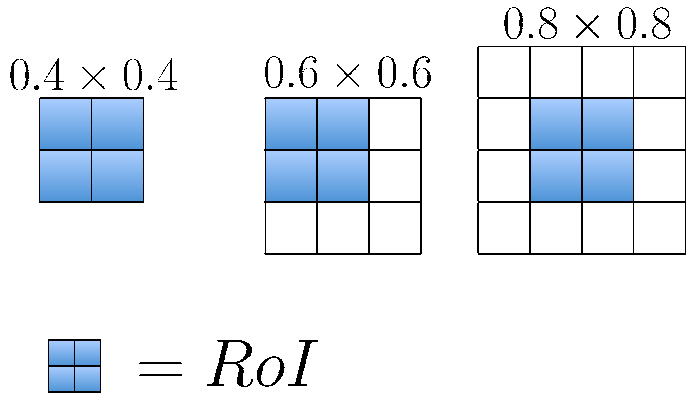

Figure 2.15: Possible choices for jet window configuration relative to a jet RoI for window sizes of 2×2, 3×3 and 4×4 jet elements.

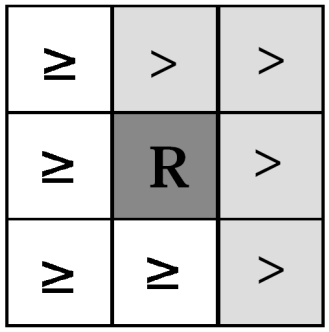

Figure 2.16: Example of criteria for RoI (labelled as R) being a local maximum. Rotations and reflections of this configuration are equivalent.

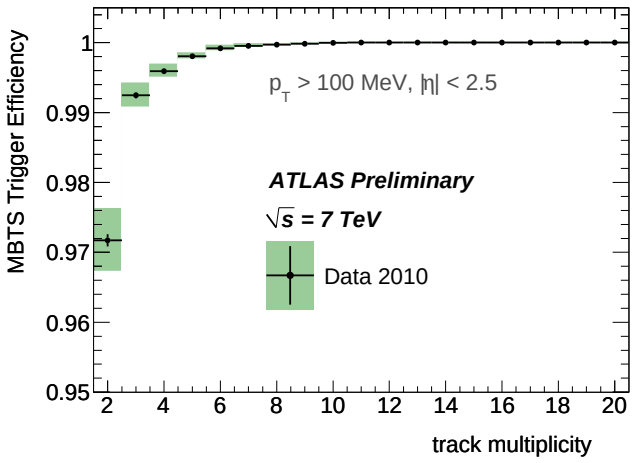

Figure 2.17: MBTS trigger efficiency as a function of number of particles.

Minimum Bias Trigger Scintillator

The Minimum Bias Trigger Scintillator (MBTS) is a detector located at high pseudo-rapidity ($2.1 < |\eta| < 3.8$) that is designed for triggering in early data taking. It consists of 16 scintillators on each side of the detector mounted between the endcap and barrel cryostats. Once the LHC is operating at nominal luminosity it is expected to sustain enough radiation damage in the first few months to become inoperable. However, currently it is being used as a trigger which is $> 99\%$ efficient for events with more than 3 reconstructed tracks, as shown in figure 2.17[24].

The ATLAS detector is the work of almost two decades of research and development, design, building, installation and commissioning. During the data taking period considered for this analysis the ATLAS detector was almost fully operational. Table 2.5[25] shows the number of channels and the percentage of them that were operational at the beginning of the LHC data taking period.

Table 2.5: Number of channels and percentage of channels operational for the sub systems of the ATLAS detector.

Detector System	Number of Channels	Percent Operational
Pixel	80M	97.5%
SCT	6.3M	99.3%
TRT	350k	98.2%
LAr EM	170k	98.6%
Tile	9800	98.0%
HEC	5600	99.9%
FCal	3500	100%
Muon	1.7M	99.6%

Chapter 3

Jet Reconstruction

This chapter describes the methods used to reconstruct jets for this analysis. The starting point for the reconstruction is energies at the cell level in the calorimeter. From this point there are three steps implemented. The first is to combine the information from the cells into larger objects which are formed around localized energy deposits in the calorimeter. This is done using a topological clustering algorithm which is explained in section 3.1. The second step, explained in section 3.2, is to run a jet algorithm to combine these clusters into jets. The final step is to perform a jet calibration, which is applied in order to correct for the non-compensating nature of the calorimeter as well as for inhomogeneities in the detector response due to, for example, transition regions between detector subsystems or regions of the detector which are not operating in the nominal configuration. This is described in section 3.3.

3.1 Topological Clustering

In order to reconstruct the response to a particle incident on the calorimeter a method know as topological clustering[26] is used. This method uses the cell energies (at the em-scale), the neighbour relationship between cells and the characteristic cell noise. The algorithm works as follows:

1. Each cell energy (E) is compared to the stored value for that cell's characteristic noise (σ). If $\frac{|E|}{\sigma} > 4$, the cell is used as a cluster seed and is included in the cluster. The absolute value of the energy is used in order to not bias the result towards higher values.

2. All cells adjacent, in three dimensions, to the seed cell (neighbours) which have $\frac{|E|}{\sigma} > 2$ are added to the cluster.

3. All cells neighbouring the neighbour cells (from step 2) which have $\frac{|E|}{\sigma} > 2$ are included in the cluster. NB: This step is repeated for all new neighbours until there are no cells for which $\frac{|E|}{\sigma} > 2$.

4. All neighbour cells on the perimeter of the cluster are included in the cluster in order to reduce the energy missed outside of the cluster.

This clustering method is used, as opposed to a method which uses a fixed area in η and ϕ, in order to reduce the noise contribution from cells which do not have energy deposits. As a result, clusters include a variable number of cells (N).

The energy of a cluster is given by:

$$E_{cluster} = \sum_{i=0}^{N} E_i^{cell} \tag{3.1}$$

and the cluster's η and ϕ values are determined by calculating the energy weighted barycentre, i.e.

$$\eta_{cluster} = \frac{\sum_{i=0}^{N} E_i^{cell}\eta_i^{cell}}{\sum_{i=0}^{N} E_i^{cell}} \tag{3.2}$$

and

$$\phi_{cluster} = \frac{\sum_{i=0}^{N} E_{cell}\phi_i^{cell}}{\sum_{i=0}^{N} E_i^{cell}} \ . \tag{3.3}$$

The clusters are treated as massless and their 4-momenta are calculated and then used as inputs into a jet algorithm.

3.2 Anti-k_T Jet Algorithm

The anti-k_T jet algorithm [27] is a modification of the k_T jet algorithm [28]. These algorithms cluster objects with 4-momenta into jets. Consider beginning with a collection of particles with known 4-momenta. A list is made of these particles. For each element of the list, i, two "distances" in p_T, y and ϕ space are considered. The first distance is d_{ij}, which is actually a set of distances, one relative to each other element

of the list, j, and is defined by

$$d_{ij} \equiv \min((p_{T,i})^{2p}, (p_{T,j})^{2p}) \frac{\Delta_{ij}^2}{R^2} \tag{3.4}$$

where

$$\Delta_{ij}^2 = (y_i - y_j)^2 + (\phi_i - \phi_j)^2 \tag{3.5}$$

and R is a distance parameter which has two default ATLAS values, 0.4 and 0.6. The larger value, 0.6, is used in this analysis since in the low luminosity running from which the dataset used here originates, the amount of pileup energy (which is due to multiple interactions during a single interaction of the proton bunches) added to the jet is negligible, and the large jet size reduces the risk of missing energy outside of the jet. The other distance (d_{iB}) defined relative to the beam axis, is given by:

$$d_{iB} \equiv (p_{T,i})^{2p} \ . \tag{3.6}$$

Both of these distances rely on terms with an exponent of $2p$. For the k_T algorithm $p = +1$ while $p = -1$ for the anti-k_T algorithm, which is what is used in the following analysis and is the default choice of the ATLAS collaboration[29].

Once the distances are calculated, the minimum distance from the entire set of d_{ij} and d_{iB} is found. If this minimum is one of the d_{ij} then elements i and j are removed from the list and replaced by an object referred to as a "pseudo-jet", which is the combination of the elements i and j, i.e. $p_{pj} = p_i + p_j$ where p_{pj}, p_i and p_j are the 4-momenta of the peusdo-jet and the elements i and j respectively. If the minimum distance in the set is d_{iB} then the element i is taken to be a jet with 4-momentum p_i and removed from the list. The list is iterated over until there are no more elements.

An example of the resulting jet shapes is shown in figure 3.1[27] for a parton level event generated by the Herwig event generator[30]. As seen the figure, in the typical case in which there are a few hard particles and many soft particles, the anti-k_T algorithm ($p = -1$) favours configurations in which the soft particles are clustered around hard particles over the case in which soft particles are clustered together. In the case where a hard particle has no other hard particle within a distance $2R$ the final jet will include only the hard particle plus the accumulation of the soft particles within a cone of radius R. In the case in which two hard particles are separated by a distance $> R$ and $< 2R$ two jets will be formed with the jet around the higher p_T particles being conical and the jet around the lower p_T particle being conical minus the overlap between the jets. The case in which two hard particles are within a distance less than R they will be merged into one conical jet along with the included soft particles. This algorithm therefore produces jets whose shape is not dependent on soft particles but rather only on the high p_T objects. This is a consequence of choosing $p = -1$ as opposed to the k_T algorithm which chooses $p = +1$.

Figure 3.2[31] shows an example event, recorded by the ATLAS detector, in which two jets have been reconstructed and clear collimated groups of particle tracks are seen. The upper-left and lower-left panels show $R - \phi$ and $R -$ z projections respectively and the upper-right panel shows the calorimeter cell energies as a function of η and ϕ.

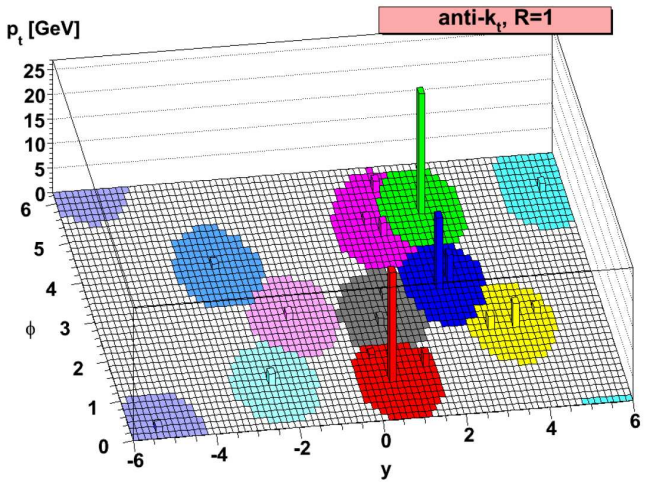

Figure 3.1: Example result of anti-k_T clustering algorithm, run on a Herwig generated QCD event, showing the grouping of energy in conical distributions around the high energy objects.

3.3 Jet Calibration

The ATLAS calorimeter measures jet energies at the em-scale. Since, in general, jets have both an electromagnetic and a hadronic component a calibration needs to be applied in order to estimate the actual jet energy. Once the em-scale jet energy has been calibrated the jet energy is said to be at the hadronic-scale (although there is no assumption made that the jet is exclusively composed of hadronic showers).

3.3.1 Numerical Inversion

The method currently used to calibrate the jets as measured by the calorimeter at the em-scale is referred to as numerical inversion[32]. This method relies exclusively

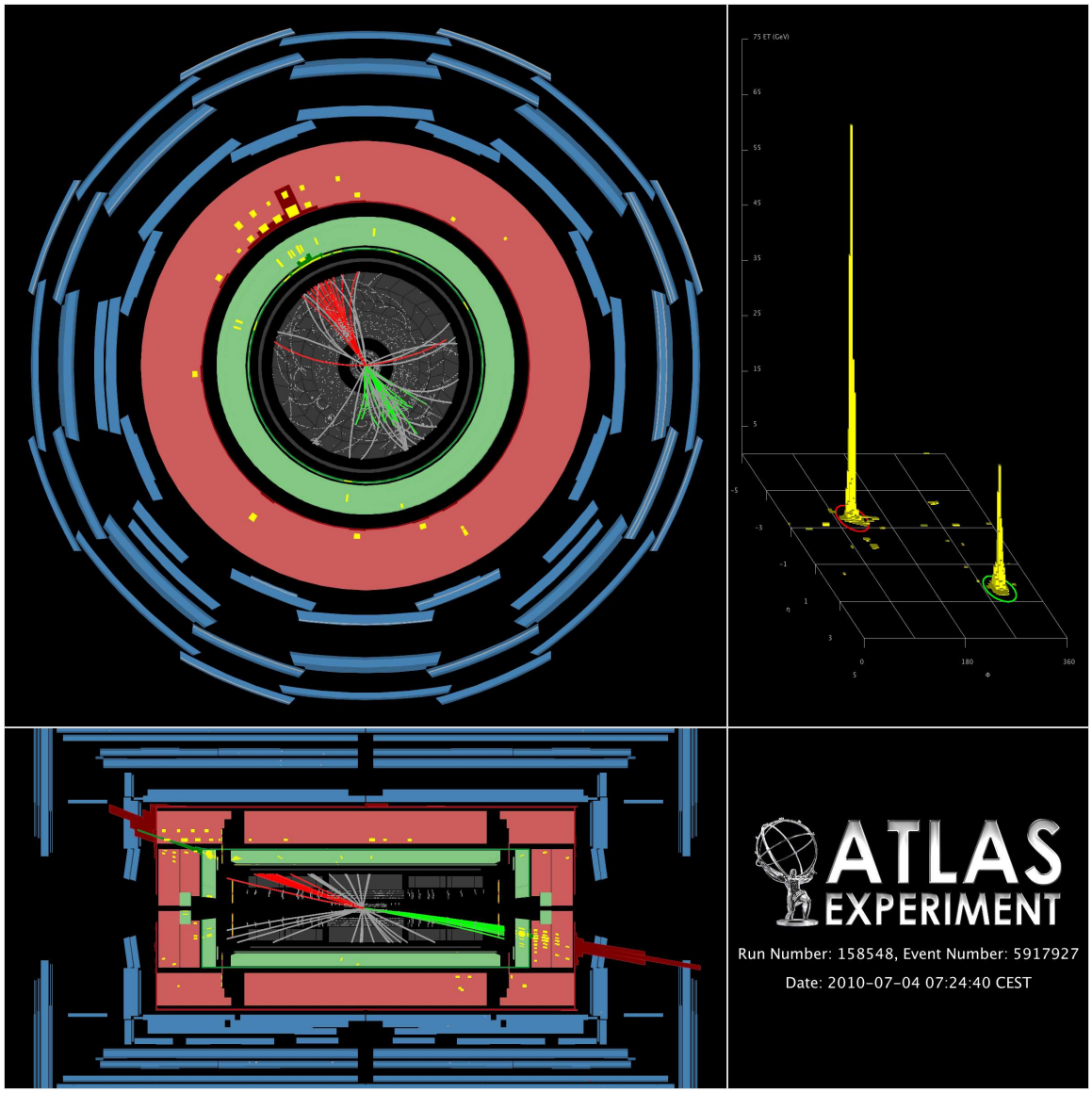

Figure 3.2: Two jet event recorded in the ATLAS detector. The upper-left and lower-left panels show $R-\phi$ and $R-$ z projections respectively and the upper-right panel shows the calorimeter cell energies as a function of η and ϕ.

on a Monte Carlo (MC) simulation of the ATLAS detector*. The terms "full-sim" and "truth" will be used in the following. Full-sim jets are the result of running the anti$-k_T$ jet finding algorithm on the simulated output of the detector (including a full simulation of the detector response), while the truth jets are the result of running the same jet algorithm on the MC particles themselves, with no detector simulation (i.e. the output of an event generator). The full-sim jets are the MC representation of what is measured by the detector and the truth jets are the MC representation of particle jets which we are attempting to measure. Note that the full-sim jet energies are at the em-scale. In the following, a quantity labelled as "FS" or "Truth" refers to a quantity made with either full-sim or truth jets respectively.

The principle of this method is to use the differences between the truth and the full-sim to extract a correction, as a function of p_T, to apply to the data to give a measure of the hadronic-scale p_T. This correction is essentially an inversion of the response function

$$R(p_T^{FS}) \equiv \frac{p_T^{FS}}{p_T^{Truth}} \, . \tag{3.7}$$

In order to determine this response function first a response function as a function of p_T^{Truth} is found, $R(p_T^{Truth})$. This is constructed by first filling a 2-D histogram with y-axis $R = p_T^{FS}/p_T^{Truth}$ and x-axis p_T^{Truth}. This 2-D histogram is projected in bins of p_T onto the x-axis and fit to Gaussian distributions. The width of these Gaussian distributions are then plotted versus the average p_T^{Truth} of the bin. A function

$$\sum_{i=0}^{4} \frac{a_i}{(ln(p_T[GeV]))^i} \tag{3.8}$$

*In the future, methods will be developed to extract this calibration using data, however, there is an insufficient amount data, at this point in time, to be able to do this.

is fit to this distribution (with 5 free parameters a_i) and the resultant fit is taken as $R(p_T^{Truth})$. This function $R(p_T^{Truth})$ is the response as a function of p_T^{Truth}, therefore p_T^{FS} can be estimated by

$$p_T^{FS} = R(p_T^{Truth}) \cdot p_T^{Truth} \ . \tag{3.9}$$

Now the 2-D histogram from above is refilled with the same value for R but as a function of p_T^{FS} which has been calculated from equation 3.9. This 2-D histogram is fit to Gaussians in bins of p_T as above and the resulting response function is fit to equation 3.8 yielding a functional form for $R(p_T^{FS})$. The calibrated transverse momentum p_T^{calib} is finally given by

$$p_T^{calib} = \frac{p_T^{FS}}{R(p_T^{FS})} \ . \tag{3.10}$$

This procedure is performed in 5 bins in $|\eta|$ resulting in a calibration which is a function of both p_T and η. The amount that the em-scale jets are calibrated in order to bring them to the hadronic scale is called the jet energy scale (JES). The correction $1/R$ is shown, for two η bins in figure 3.3[33].

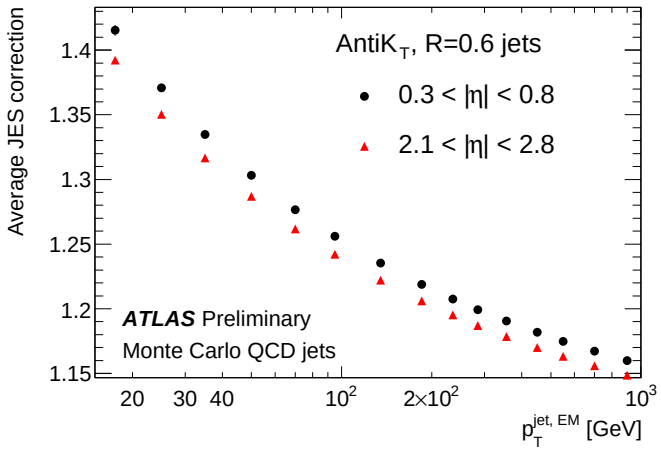

Figure 3.3: Jet energy scale correction for two example bins in η.

3.3.2 Jet Energy Scale Uncertainty

It is a substantial effort to estimate the uncertainty on a jet calibration which is taken from MC. In order do so, the systematic effects which feed into this uncertainty have been simulated[33]. The idea is to vary parameters in the MC simulation to estimate the effect on the jet energy reconstruction. The effects studied are:

Dead material The amount of dead material (uninstrumented material outside of the calorimeter into which particles can deposit energy which is not measured by the calorimeter) between the interaction point and the calorimeter can have an effect on the overall jet energy scale. An increase in the dead material of up to $0.2X_0$ (radiation lengths) was simulated to study this effect. This corresponds to an increase in the amount of dead material of approximately 10%.

Noise thresholds A difference between the noise values used in the MC and data could affect the results of the topological clustering algorithm. To see this effect, jets were reconstructed with the topological clustering signal to noise thresholds varied by $\pm 10\%$. This is a conservative estimate based on observations of the noise stability which is typically $< 1\%$ in the EM[34] and tile[35] calorimeters.

Beam spot Jets are nominally reconstructed assuming that the beam spot position is at $(x, y, z) = (0, 0, 0)$. The simulation was rerun using a beam spot at $(x, y, z) = (1.5, 2.5, -9.0)$ mm to show the effects of a displaced beam spot. This conservative estimate is more than three times the beam spot displacement seen in the data set used, which had a beam spot position that remained relatively stable.

Absolute em-scale energy An uncertainty of 3% on the absolute em-scale energy was assumed for the EM calorimeter. This number is derived from the difference in response between test beam data and MC, and the time stability of the electromagnetic scale estimated by variations in the electronics behaviour over time.

Closure of numerical inversion The inherent uncertainty in the numerical inversion technique was estimated as the discrepancy between the truth and calibrated spectra after the numerical inversion was applied. This effect was seen to be $\leq 1\%$.

Hadronic shower model In order to assess the effect of different hadronic showering models the simulation was rerun switching from the nominal model (QGSB + BERTINI) to two other models, QGSB and FTFP + BERTINI. The former does not use Bertini nucleon cascades and the latter substitutes the Quark Gluon String fragmentation model with the Fritiof model.

Monte Carlo event generator To assess the effect of different Monte Carlo event generators the simulation was rerun using two non-nominal tunes of the Pythia event generator, one with a different model of the underlying event and one which has parameters tuned from LEP data. The simulation was also rerun using an independent generator (ALPGEN + HERWIG).

More details regarding the changes to the hadronic shower model and the MC event generators can be found in [33]. The estimated systematic effects above, which are assumed to be uncorrelated, are combined and the resulting uncertainty on the jet calibration which depends on p_T and $|\eta|$. This relative uncertainty is shown in figure

3.4 as a function of p_T and $|\eta|$. The JES uncertainty is $\sim 10\%$ at the lowest values of p_T and decreases to $\sim 5\%$ for values $> 60\,\text{GeV}$. The JES uncertainty is approximately flat as a function of $|\eta|$ for $|\eta| < 2$ and increases slightly for $|\eta| > 2$. Note that this JES uncertainty estimation is only valid for $p_T > 20\,\text{GeV}$ and $|\eta| < 2.5$. As will be seen in chapter 5 these limitations are of no concern for the analysis presented here.

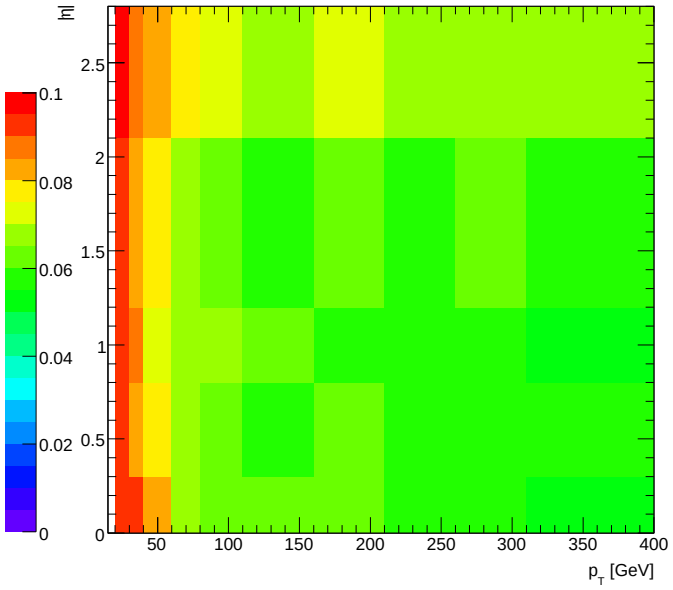

Figure 3.4: Relative jet energy scale uncertainty as a function of $|\eta|$ and p_T.

Chapter 4

Data and Monte Carlo

This chapter outlines the details of the data set which was collected and used for this analysis. The data were collected over the period from 30 March 2010 to 4 June 2010 which corresponds to the beginning of the LHC 7 TeV physics run.

The data recorded by ATLAS are split up into "luminosity blocks" (lumi blocks) which correspond to the data recorded during a period of 2 minutes. The data are separated into lumi blocks because the LHC instantaneous luminosity changes as a function of time, as can the state of the ATLAS detector subsystems. With the data separated into time durations shorter than a full run (which can be ≈ 1 day) a more accurate integrated luminosity calculation can be made, and a selection can be made to choose only data which have been taken with the ATLAS detector in the desired state. Details of how the integrated luminosity is calculated and how the state of the ATLAS detector is recorded (this is known as "data quality") can be found in sections 4.1 and 4.2.

After the appropriate lumi blocks are identified based on the data quality information, further selection is made to choose specific events for the analysis, as will be described in section 4.3, and cuts are applied in order to accept only "good" jets, as detailed in section 4.4. A brief description of the Monte Carlo simulated data is also included in this chapter, in section 4.5.

4.1 Data Quality

In order to keep track of the status of each component of the ATLAS detector, which can change as a function of time, data quality flags are used for each sub-detector. These flags indicate whether each sub-detector is in the nominal state (flag status = GREEN), a non-nominal status which either does not have a major effect on the data or can be fixed offline (flag status = YELLOW) or the sub-detector is in a state in which the data are not useable (flag status = RED). The data quality flags are determined from a series of comparisons to the expected state of the detector. The properties considered include, for example, electronics status (both readout and power), high voltage status, detector noise, database values and accessibility and basic detector performance. A flag may be set to YELLOW for a sub-system if, for example, it is operating at a non-nominal voltage. A RED data quality flag could be assigned if, for example, there is a dead power supply which completely disables the instrumentation in some part of the detector. The data quality flags are stored for each lumi block of each run and can be accessed via the ATLAS Run Query tool[36] which searches the run meta-data and returns a list of run numbers and lumi blocks which meet specified data quality criteria. The Run Query tool also

Table 4.1: Data quality flag and LHC status requirements.

DQ Item	Flag
LHC Beam	STABLE
LHC Beam Energy	3.5 TeV
Pixel Detector	GREEN
SCT	GREEN
LAr Calorimeter	GREEN
Tile Calorimeter	GREEN

retrieves information regarding the status of the LHC. The data quality and LHC status requirements used for this analysis are summarized in table 4.1. The LHC "STABLE" status denotes that the beams are in a state such that it is unlikely that the control of the beams will be lost. This status is dictated by LHC control and the solid state subsystems of the ID are not brought to nominal operating voltages until it is set to STABLE. The corresponding run numbers and luminosity blocks used in this analysis are listed in table 4.2.

4.2 Integrated Luminosity

Although the observable defined to examine the azimuthal decorrelation is chosen to be a normalized differential cross section which is not dependent on the total amount of data taken (see chapter 5) it is still useful to know the total integrated luminosity $\int \mathcal{L}dt$, which is the instantaneous luminosity ($\mathcal{L}$) integrated over the data taking time, where $\mathcal{L}$ is the interaction rate per unit cross section, given in units of flux ($\mathrm{cm}^{-2}\mathrm{s}^{-1}$) which is $\mathcal{O}(10^{29}\ \mathrm{cm}^{-2}\mathrm{s}^{-1})$ for this data set.

In order to calculate the integrated luminosity a Van Der Meer scan[37] was performed. This method measures a visible cross section (σ_{vis}) for some detector which

Table 4.2: Run numbers and corresponding luminosity blocks used in this analysis.

ATLAS Run Number	$\int \mathcal{L}dt$ [nb^{-1}]	Lumi Block Range
156682	1.41	396-514
155697	4.33	264-506
155678	1.21	241-308
155669	0.53	257-311
155634	1.13	144-147 & 149-333
155160	1.36	240-503
155116	0.57	8-93
155112	3.68	127-166 & 186-625
155073	1.20	82-407
154822	0.43	177-365
154817	0.57	9-287
154813	3.41	8-20 & 40-49 & 83-187
Total:	19.55	

acts as a counter. Once σ_{vis} is determined it can be combined with the measured counting rate for the detector (R) to give the instantaneous luminosity by

$$\mathcal{L} = \frac{R}{\sigma_{vis}} \, . \tag{4.1}$$

Therefore by calculating σ_{vis} for a detector (which should be constant for a given beam energy) the luminosity can be found at any time by measuring the event rate. The quantity σ_{vis} can be measured with the colliding proton beams by physically moving them through each other incrementally and recording the counting rate for each position. In an example case as described in [38] the counting detector used is the MBTS and the corresponding visible cross section denoted by σ_{vis}^{MBTS} was found to be

$$\sigma_{vis}^{MBTS} = (50.5 \pm 5.4) \text{ mb}. \tag{4.2}$$

The total integrated luminosities for each run used are listed in table 4.2.

4.3 Event Selection

After data quality selection on lumi blocks, a further selection is made on an event by event basis. The first selection accepts only events in which there are two or more reconstructed jets. As the following analysis focuses on angles between jets there is no need to keep events which have fewer than two. This selects only a small subset of the events which pass the data quality criteria, greatly reducing the data file size and reducing the computing time of the analysis.

The second event selection is a trigger selection which requires that the L1_J5 trigger has been satisfied. In order to ensure that there is no bias introduced into the analysis, the trigger efficiency of the L1_J5 trigger is estimated from data. This is done by making a trigger turn on curve from a comparison of the L1_J5 trigger with the MBTS trigger under the assumption that the latter is fully efficient over the turn on of the L1_J5 trigger.

Trigger efficiency curves are shown in figure 4.1[39]. These distributions show the efficiency of the L1_J5 trigger as a function of p_T and η. The trigger efficiency is calculated by taking the ratio of two p_T (or η) distributions. The denominator is the p_T (or η) distribution made from all of the events which pass the MBTS selection. The numerator is the p_T (or η) distribution made from all jets which are matched to a level-1 RoI within a cone of $\Delta R < 0.4$ where $\Delta R \equiv \sqrt{\Delta\eta^2 + \Delta\phi^2}$. The efficiency as a function of jet p_T is $\approx 100\%$ for $p_T > 60\,\text{GeV}$ and correspondingly, the efficiency as a function of η with a cut of $p_T > 60\,\text{GeV}$ is $\approx 100\%$ and flat as a function of η. Note that the analysis described in chapter 5 requires all events to have at least one jet in this fully efficient region of the L1_J5 trigger. These efficiencies also agree with

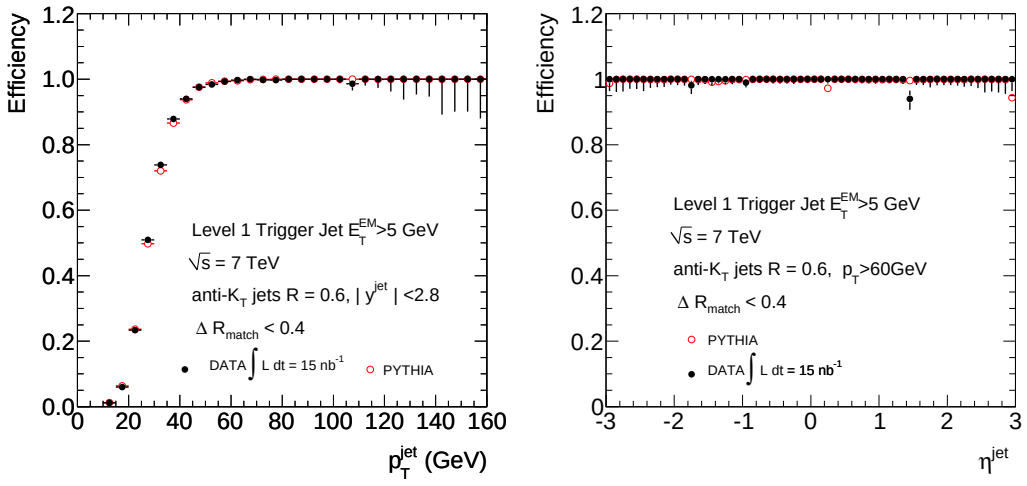

Figure 4.1: Trigger efficiency for the L1_J5 jet trigger as a function of p_T and η. Trigger efficiencies are $\approx 100\%$ for $p_T > 60\,\text{GeV}$.

Table 4.3: Number of events passing each stage of the event selection.

	# of Events	Fraction
Total events with ≥ 2 jets	13629475	1
L1_J5 trigger passed	3361846	0.247
Vertex cut passed	3328705	0.244

the prediction from the PYTHIA simulated Monte Carlo data set which is described in section 4.5.

The final event selection which is made is to require that for each event there is at least one reconstructed vertex that contains at least five tracks. This criterion ensures that an event corresponds to a proton-proton collision and not to noise or other backgrounds.

The number of events which pass each of the event selection criteria is listed in table 4.3.

4.4 Jet Selection

Jets were reconstructed using an anti-kt jet finding algorithm, as described in section 3.2. These jets have been calibrated using the numerical inversion technique, detailed in section 3.3 and are thus at the hadronic energy scale. After reconstruction a set of quality cuts[40] are applied in order to remove "jets" which were reconstructed based on clusters which were seeded by cells which show high energies due to calorimeter noise or from cosmic rays. There are four jet variables which are cut on. These are:

N90 Numer of cells which contain 90% of jet's energy.

Quality The fraction of a jet's energy which comes from cells which have a poor agreement between the predicted pulse shape and the measured pulse shape for that event according to the OFC χ^2 variable.

Electromagnetic fraction (EMF) The fraction of the jet's energy which is deposited in the electromagnetic calorimeter layers.

Timing Cell-energy-squared-weighted time of all the cells in the jet, ie: $\frac{\sum_{cells} E_{cell}^2 t_{cell}}{\sum_{cells} E_{cell}^2}$, where E_{cell} is the cell energy at the em-scale and t_{cell} is the cell time.

Table 4.4 shows the values of the cuts which are made on the these variables, in the order in which they were made. A jet that is composed mostly of energy from a few noisy cells will not pass the N90 cut. There are rare occasions in which the LAr calorimeter has "noise bursts" which consist of a group of LAr cells which exhibit a

Table 4.4: Jet quality cuts.

Jet Quality Cut
N90 ≥ 5
Quality < 0.8 & EMF < 0.95
abs(Timing) < 50 ns

coherent noise for a short period of time. The simultaneous cuts on Quality and EMF are intended to reject jets from these type of events. Most of the cosmic ray muons passing through the detector are minimum ionizing and leave only a small amount of energy in calorimeter cells which is insufficient for a jet to be reconstructed. However, in the rare situation in which a cosmic ray deposits a large amount of energy via Bremsstrahlung radiation, an energetic jet can be reconstructed. In this case the energy is not, in general, in time with the LHC collision and is contained within a small number of cells and will be rejected by the timing and/or the N90 cut. Figures 4.2, 4.3 and 4.4 show the cut flow of the jet cuts as a function of track η, ϕ and p_T. Cuts are applied in the order indicated in the legend with each distribution showing the events which have passed the cuts cumulatively. None of the cuts remove a large number of jets but the N90 cut's effect on the p_T spectrum is significant since the jets are removed from the high p_T region. The other cuts remove a small number of jets uniformly over the the distributions resulting in little visible effect. These cuts are standard for ATLAS jet analyses.

4.5 Monte Carlo Data

Aspects of this analysis require using a Monte Carlo (MC) simulated data set. These data use PYTHIA 6.4.21[41] to simulate the parton-parton hard scattering process,

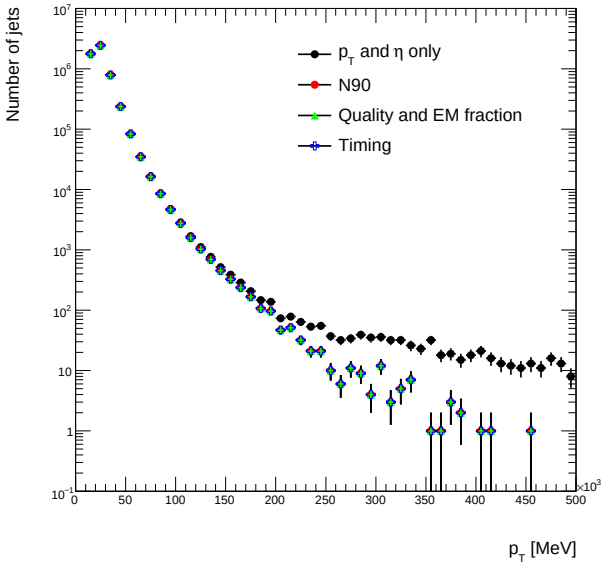

Figure 4.2: Jet p_T showing cut flow of jet quality cuts. The N90 cut has an effect at high P_T while the other cuts show a negligible effect.

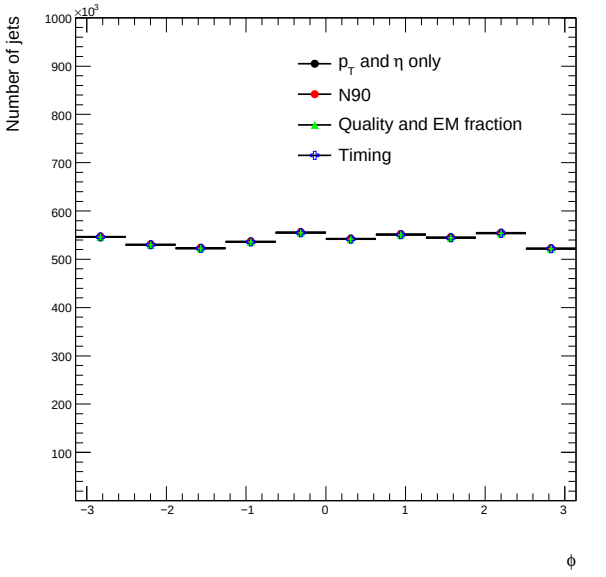

Figure 4.3: Jet ϕ showing cut flow of jet quality cuts. The cuts remove a small number of event uniformly which has a negligible effect on the distribution.

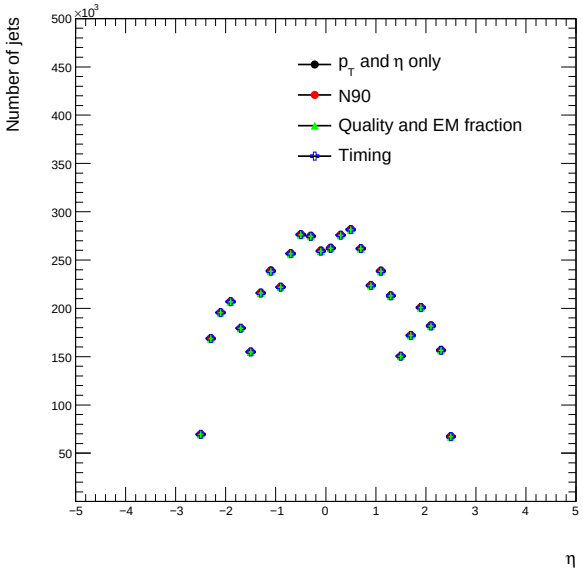

Figure 4.4: Jet η showing cut flow of jet quality cuts. The cuts remove a small number of event uniformly which has a negligible effect on the distribution.

showering and hadronization. Details of how PYTHIA performs these predictions can be found in chapter 6. Pythia contains numerous tuneable parameters. The choice the values for these parameters for this analysis is standard for the ATLAS simulation. After the PYTHIA simulation has been performed the resultant particles' interactions with the detector are simulated using GEANT4[42]. This GEANT4 simulation[43] includes all the components of the ATLAS detector including non-active material (for example: cabling, mechanical supports or cryostat walls) as well as a simulation of the full electronics system of the read-out of each component of the detector. The resulting simulated data are a representation of the data output of ATLAS, and are in the same format. In some cases it is useful to use only the data produced by PYTHIA and not to use the GEANT4 simulation of the detector, in order to have a simulated data set that represents the final state of a physics process without the effects of the detector.

Table 4.5: Monte Carlo data set components.

p_T Range [GeV]	Number of Events	Cross Section [nb]	$\int \mathcal{L}dt$ [nb^{-1}]
8-17	399993	9.75×10^9	4.10×10^{-5}
17-35	395793	6.73×10^8	5.88×10^{-4}
35-70	399691	4.11×10^7	9.71×10^{-3}
70-140	393891	2.19×10^6	1.80×10^{-1}
140-280	388944	8.73×10^4	4.46
280-560	391289	2.33×10^3	1.68×10^2
560-1120	385341	3.34×10^1	1.15×10^4

In order to cover a wide range in transverse momentum numerous MC data sets were generated with different ranges in transverse momentum*. Since the jet production cross section decreases very rapidly as a function of increasing p_T, many component MC data sets are used to provide a broad range in p_T without having to generate an unreasonable amount of MC nor having to use a complicated event weighting scheme. Table 4.5 summarizes the seven MC data set components which make up the total MC data set used in this analysis. The effective integrated luminosity is shown for each component.

*The p_T of each range refers to the average p_T of the two initial outgoing partons resultant from the hard scattering simulation. This does not represent the p_T value of the outgoing jets exactly.

Chapter 5

Analysis

5.1 Observable

The azimuthal decorrelation is measured using the varible $\Delta\phi$, defined as the angle between the projections, onto the transverse plane, of the momenta of the two highest p_T jets in the event, as illustrated in figure 5.1. For ease of notation the leading and second leading jet, based on p_T, will be denoted j_1 and j_2. The angle is always chosen to be the smaller of the two possible angles between j_1 and j_2 resulting in a range for $\Delta\phi$ of $0 \rightarrow \pi$ radians. The observable is then defined as a normalized differential cross section $\frac{1}{\sigma_{tot}}\frac{d\sigma}{d(\Delta\phi)}$ where the normalization $\frac{1}{\sigma_{tot}}$ is the inverse of the total number of events used to make the distribution. This normalized differential cross section is plotted versus $\frac{\Delta\phi}{\pi}$ and is scaled by the inverse of the bin width of each bin giving a value per radian. The value of $\frac{\Delta\phi}{\pi}$ is not taken as the bin centre, but rather, as the average value over the bin, as these two values can differ significantly in this rapidly

changing distribution. Only events are chosen in which the transverse momentum of j_1 and j_2 are above a minimum p_T value and both of the leading jets fall within a specified range in rapidity. Table 5.1 shows the values of these cuts for this analysis. The cut on the jet p_T ensures that the jets considered are of a high enough p_T to be on the fully efficient part of the trigger efficiency curve. The rapidity cut, which limits the jets to the central region of the detector is chosen in order to limit the variance in the detector response which is expected as the detector geometry varies as a function of rapidity.

Figures 5.2, 5.3 and 5.4 show the j_1 and j_2 distributions, for data and MC, for the transverse momentum (p_T), rapidity (y) and azimuthal angle (ϕ) respectively. The MC distributions have been normalized to the number of events in data. The p_T data distribution shows jets with p_T values up to $\approx 400\,\text{GeV}$. The y and ϕ distributions are flat over the range considered. The agreement between data and MC is within the statistical errors shown.

Figure 5.5 shows the raw $\Delta\phi$ distribution from data showing only the statistical errors. This distribution is made from jet quantities as measured by the ATLAS detector and has not been corrected to account for detector effects (this correction is known as unfolding and is discussed in detail section 5.2), nor are systematic errors shown. The following sections detail the unfolding corrections and the assessment of systematic errors.

Table 5.1: Jet kinematic cuts.

Cut
$p_{T,1} > 70$ GeV
$p_{T,2} > 50$ GeV
$-0.8 < y < 0.8$

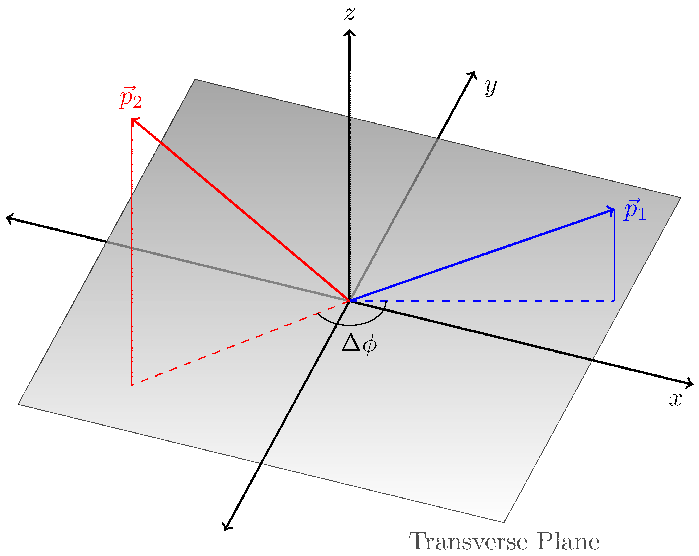

Figure 5.1: Definition of azimuthal angle $\Delta\phi$ which lies in the range $[0, \pi]$.

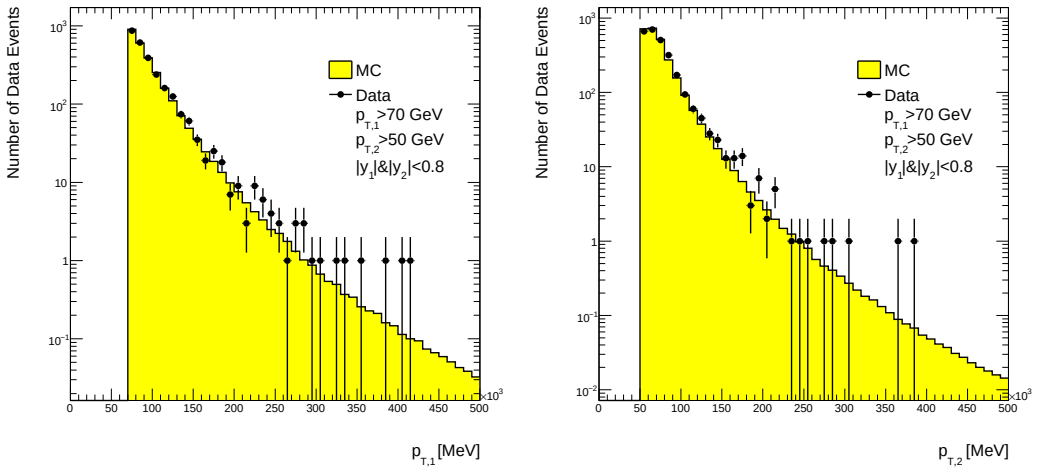

Figure 5.2: Transverse momentum distributions for leading and second leading jets. MC spectrum is normalized to the number of events in data.

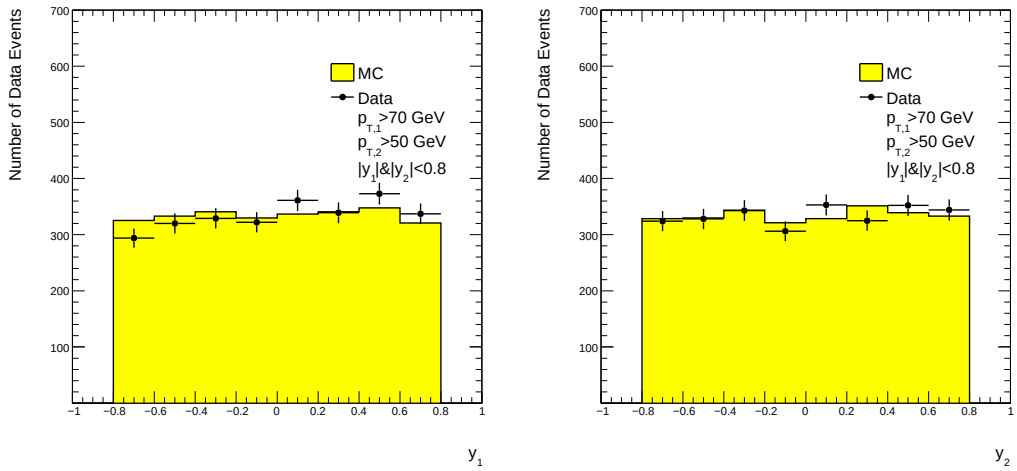

Figure 5.3: Rapidity distributions for leading and second leading jets. MC spectrum is normalized to the number of events in data.

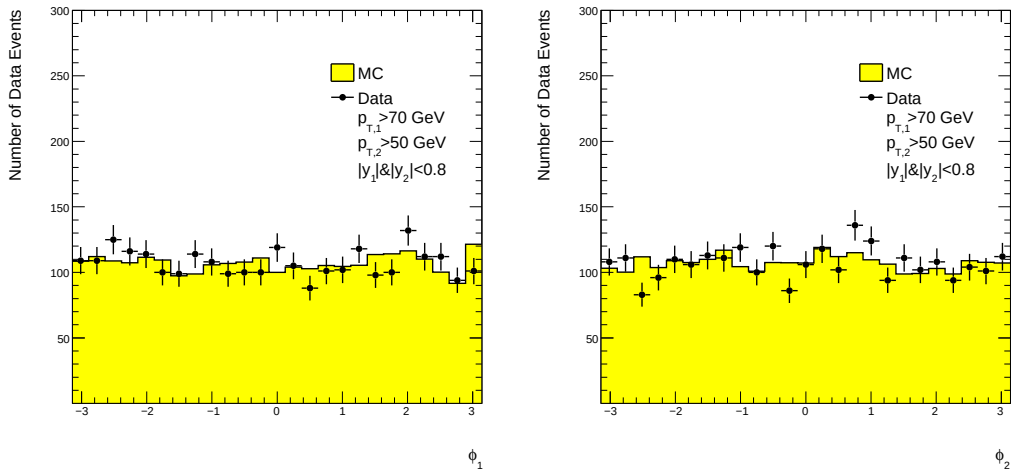

Figure 5.4: Azimuthal angle distributions for leading and second leading jets. MC spectrum is normalized to the number of events in data.

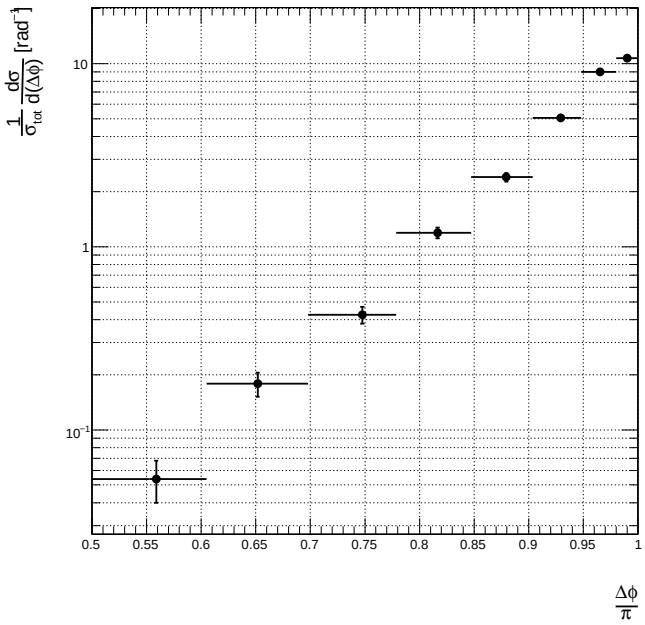

Figure 5.5: Normalized differential $\frac{1}{\sigma_{tot}}\frac{d\sigma}{d(\Delta\phi)}$ cross section with no unfolding corrections, statistical errors only.

5.2 Unfolding

The goal of this analysis is to provide a measurement which is independent of the ATLAS detector. That is, to provide a result which best represents physical phenomena independent of the detector. In this case an unfolding is performed in order to correct the final $\Delta\phi$ spectrum from what is measured by the ATLAS detector to one that represents the particle jets, after hadronization, incident on the detector. This gives a result which is ATLAS-independent.

The difference between the measured spectrum and the particle jet spectrum is due to the fact that the detector does not measure the kinematic jet properties perfectly. When a kinematic jet quantity is measured by the detector there is some associated

uncertainty. For example consider some kinematic variable X'. For a large number of jets incident on the detector with exactly the same value $X' = x'$ the measured values will make up some distribution X with mean μ_x and characteristic width σ_x. The width of this distribution (σ_x) is known as the resolution. The difference between the measured values and the true values of the jets' p_T, y and ϕ change the $\Delta\phi$ spectrum, and it is these effects which must be corrected for in the unfolding. Note that these effects are not just due to the uncertainty associated with the inherent detector response but can also be due to gaps in instrumentation, dead material in the detector, hardware defects or other detector anomalies.

The information for the unfolding is taken from the ATLAS Monte Carlo simulation (see chapter 4 for details). The "full-sim" jets are the result of running the anti-k_T jet finding algorithm on the simulated output of the detector, while the "truth" jets are the result of running the same jet algorithm on the generator level MC particles themselves. The full-sim jets are the MC representation of what is measured by the detector, while the truth jets are the MC representation of the particle jets of which we are attempting to measure the properties. In the following, a distribution labelled as "Full-sim" or "Truth" refers to the distribution being made with either "full-sim" or "truth" jets.

Figure 5.6 shows the ratio of the full-sim to the truth $\Delta\phi$ distributions which is an estimate of the amount of unfolding which needs to be performed. Figure 5.7 shows the "migration matrix" for $\Delta\phi$ from truth to full-sim, M_{ij}, which gives the probability of an event which has a $\Delta\phi_{Truth}$ value in bin i to have a $\Delta\phi_{Full-sim}$ value in bin j. The matrix M_{ij} is normalized such that $\sum_j M_{ij} = 1$.

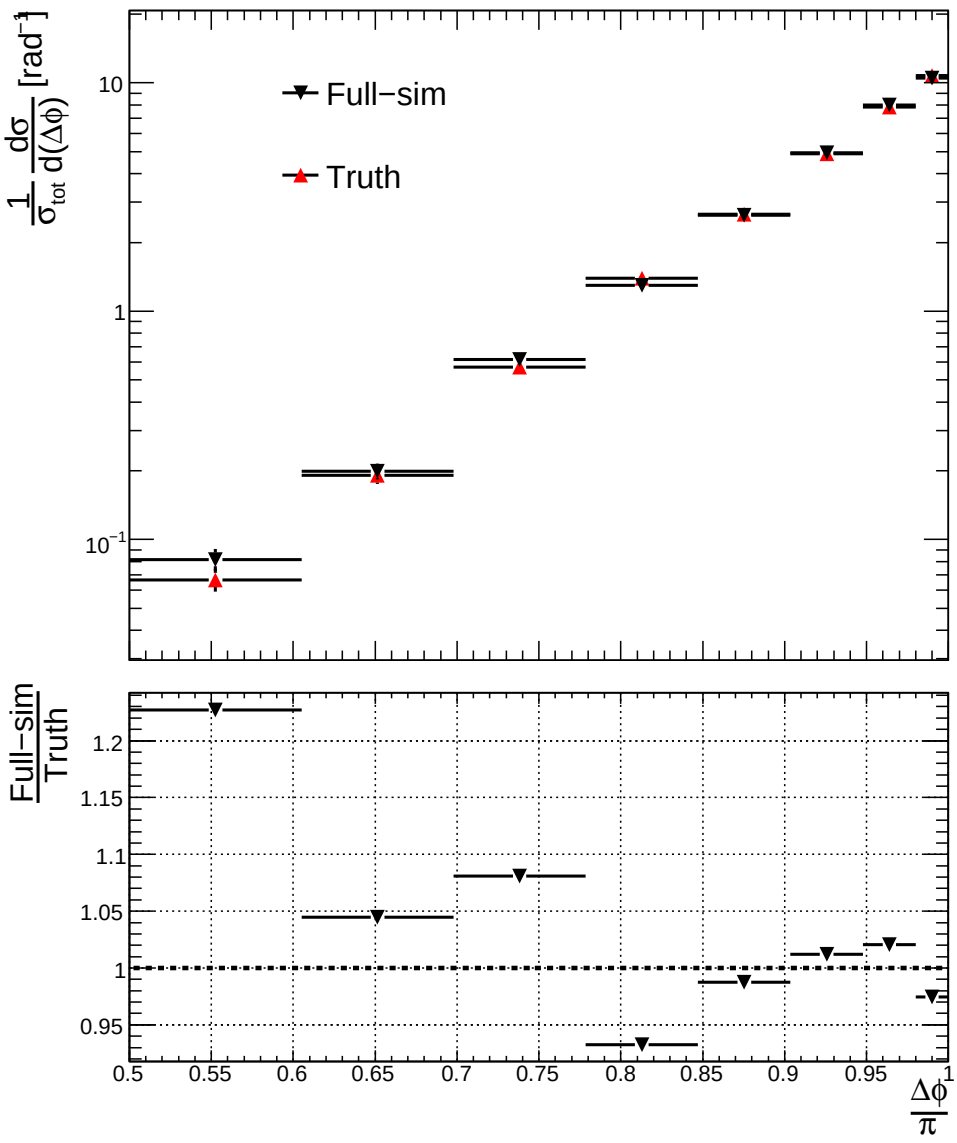

Figure 5.6: (above) Full-sim and truth $\Delta\phi$ distrubutions. (below) Ratio of the full-sim to the truth $\Delta\phi$ distributions. This ratio corresponds to the expected amount of unfolding required.

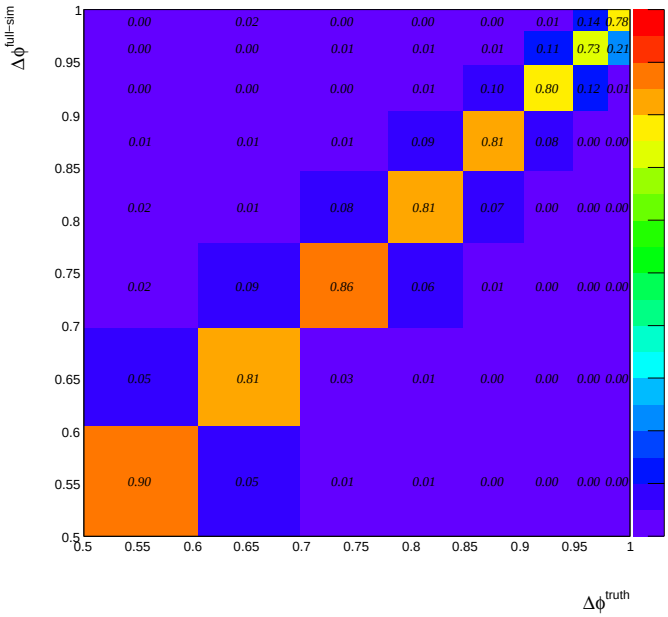

Figure 5.7: Migration matrix M_{ij}

Although the full-sim spectrum in figure 5.6 includes all of the detector effects using all the available information from the MC simulation of the detector, it is not sufficient to make the unfolding correction simply by taking the ratio the two distributions, i.e.

$$\frac{\Delta\phi_{Truth}}{\Delta\phi_{Full-sim}} \, . \tag{5.1}$$

In order for this simple ratio to give the proper unfolding correction the MC estimation of the jet distributions would have to be known to be correct; specifically, the case in which a third jet (j_3) is present in the event. In this case the distribution of the third jet's p_T and y would have to be well modelled in the MC and it is not desirable to be dependent on this. In order to understand why this is the case consider first the scenario in which there are only two jets in an event. In this case the difference between the truth and full-sim spectra would be exclusively due to detector effects

which are described by the simulation of the ATLAS detector and would not be sensitive to how well the jet kinematic distributions are represented in the event generator. In this case the simple ratio in equation 5.1 would be sufficient for an unfolding correction. However, in the presence of a third jet the situation becomes more complex. In this case the difference in the truth and full-sim spectra is due to the detector effects on the first and second jet, as before. However, in this case there is a probability that what is the truth third jet is reconstructed as the second jet in the full-sim. In this case the $\Delta\phi$ between the first and third truth jets is measured, which is not the intended measurement. Figure 5.8 shows the migration matrices for the case in which the leading two truth jets are properly identified ($M_{ij}^{\checkmark}$) as the leading two full-sim jets, and the migration matrix for the case in which the third truth jet is reconstructed to be the first or second full-sim jet ($M_{ij}^{\times}$). The former is essentially diagonal, however the latter is closer to a flat distribution, that is, showing nearly equal probability for an event with $\Delta\phi^{Truth}$ in some bin to have a $\Delta\phi^{Full-sim}$ value in any other bin. For low values of $\Delta\phi$ this can have a large effect on distribution. Figure 5.9 shows the fraction of events in which the third truth jet is found to be one of the leading full-sim jets. Given this dependence on the third jet, using the ratio in equation 5.1 would give an unfolding correction that is dependent on the MC prediction of probability of having a third jet in the event, as well as the predicted shape of the p_T and y distributions for the third jet. In order to remove this dependence a weight is applied which takes into account the kinematics of the third jet in an event (if one is present), as well as the $\Delta\phi$ between the two leading jets. This weight (W) is applied to each event and is calculated by taking the ratio of two 3-dimensional histograms in $\Delta\phi$, $p_{T,3}$ and y_3, where $p_{T,3}$ and y_3 are the transverse momentum and rapidity of the third jet, or, in the case where there is no third jet

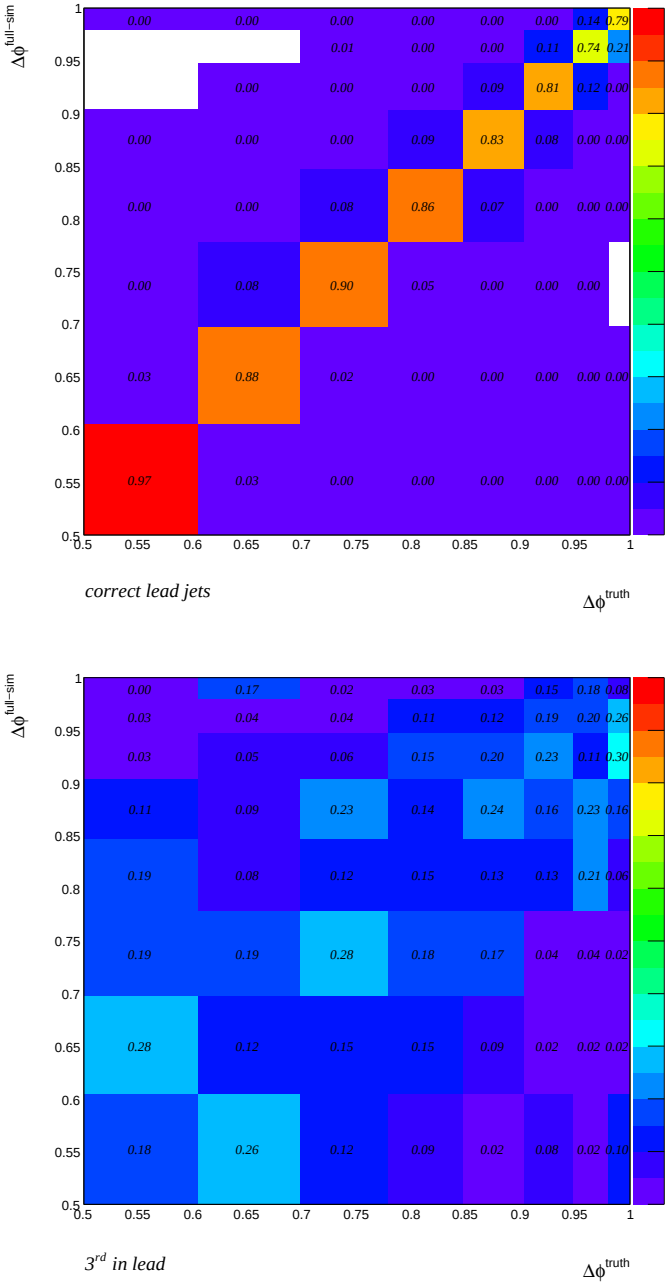

Figure 5.8: Migration matrices for events in which the third truth jet is misreconstructed as a leading jet (right), and for events in which the third truth jet is reconstructed as a leading jet (left).

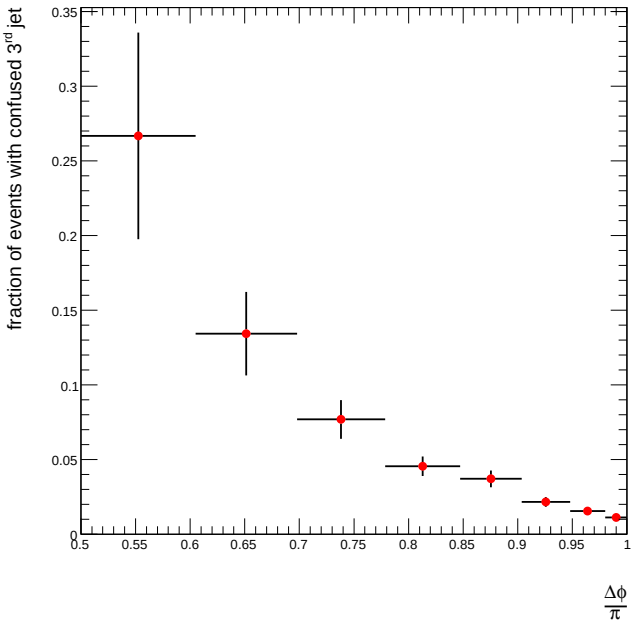

Figure 5.9: Fraction of events in which the third truth jet is reconstructed as one of the leading full-sim jets (in MC).

just by the ratio of the $\Delta\phi$ histograms, i.e.

$$W(\Delta\phi, p_{T,3}, \eta_3) = \frac{N_{truth}(\Delta\phi, p_{T,3}, \eta_3)}{N_{full-sim}(\Delta\phi, p_{T,3}, \eta_3)} \ , \ n_{jet} \geq 3 \tag{5.2}$$

$$W(\Delta\phi) = \frac{N_{truth}(\Delta\phi)}{N_{full-sim}(\Delta\phi)} \ , \ n_{jet} = 2 \tag{5.3}$$

The unfolded spectrum is then made by taking all events in data, which pass the kinematic cuts defined for the observable, and filling the $\Delta\phi$ histogram with each event getting a weight $W(\Delta\phi, p_{T,3}, \eta_3)$, or $W(\Delta\phi)$ for events with only two jets. Figure 5.10 shows the total unfolding correction on the $\Delta\phi$ spectrum. The bin corrections range in value from ≈ 0.7 to 1.05 and roughly correspond to the amount of unfolding predicted in figure 5.6.

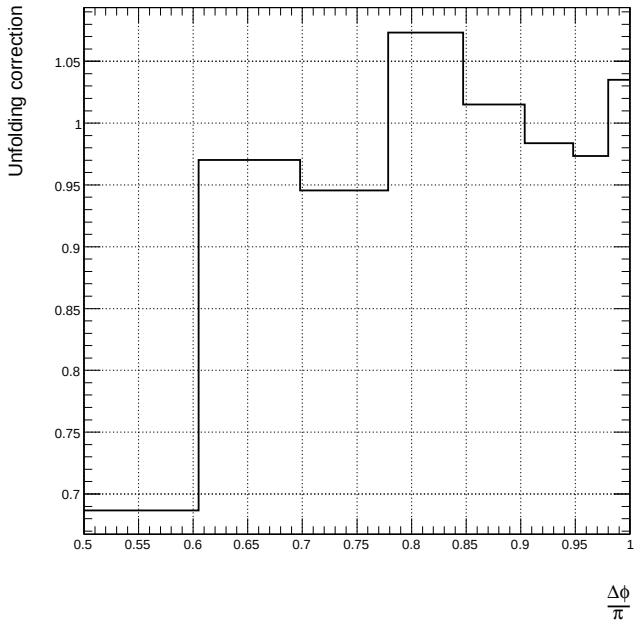

Figure 5.10: Total unfolding correction on the $\Delta\phi$ spectrum resulting from the weights described by equations 5.2 and 5.3.

5.3 Systematic Uncertainties

In order to assess the systematic error on the measurement of the $\Delta\phi$ spectrum three effects are considered. These are:

- Propagation of the uncertainty on the jet energy scale
- Effect of the inaccuracies of MC estimation of the third jet properties
- Effect of inaccuracies in the MC resolution predictions

The procedure for estimating the systematic errors due to these three effects is described below. Following these descriptions all of the errors are displayed, bin by bin, in figure 5.19.

5.3.1 JES Uncertainty

The relative uncertainty on the JES is a function of p_T and η and is shown in figure 3.4 [33]. To estimate the effect of this uncertainty on the measurement, the analysis is repeated with the unfolding histogram W (equations 5.2 and 5.3) calculated as in the standard analysis. However, before filling the corrected $\Delta\phi$ distribution, the p_T of each jet is scaled, up and down, by the uncertainty given at that value of p_T and η. This yields two new $\Delta\phi$ distributions, one for the positive and one for the negative scaling. The ratio of these spectra to the nominal corrected MC spectrum is taken, and for each bin whichever of the positive or negative scaling errors is larger is taken as the corresponding systematic error on that bin due to the JES uncertainty. Figure 5.19 includes the result.

5.3.2 Third Jet

The unfolding method detailed in section 5.2 is designed to be insensitive to how well the third jet kinematics have been modelled in the MC. To test the insensitivity, the differences between the MC prediction and the data for the third jet transverse momentum and rapidity and the number of jets is used, where cuts on the third jet minimum p_T and η range are: $p_{T,3} > 15\,\text{GeV}$ and $|\eta| < 2.5$. As in the previous section the analysis is redone, calculating the unfolding weights from the nominal MC truth and full-sim jets. However, in this case a weight (W_{jet3}) is applied to each event along with the unfolding correction. This additional event weight is derived from the discrepancies between data and MC with respect to the third jet and is in fact the product of three weights,$W_{jet3} = W^{prob}_{jet3} \times W^{p_T}_{jet3} \times W^{y}_{jet3}$. Where W^{prob}_{jet3} (=0.97) is the

data:MC ratio of the number of events with ≥ 3 jets corresponding to the probability of having a third jet in the event (see figure 5.11). $W_{jet3}^{p_T}$ is a function of the third jet's p_T and is determined by fitting a linear function to the data:MC ratio of the third jet p_T distributions (see figure 5.12). W_{jet3}^{y} is a function of the third jet rapidity and is taken directly from the ratio histogram shown in figure 5.13.

Figure 5.14 shows the ratio of the W_{jet3} weighted $\Delta\phi$ spectrum to the nominal $\Delta\phi$ spectrum. This corresponds to the error which would be associated with using the simple ratio unfolding in equation 5.1. This figure also shows the estimated systematic error on the unfolding which takes the third jet into account. This systematic is calculated by comparing how well the unfolding of the MC full-sim spectrum reproduces the original MC truth input with the event weights, W_{jet3}, relative to how well the unfolding works in the nominal analysis, i.e.:

$$\frac{\Delta\phi_{Corr}^{Weighted}}{\Delta\phi_{Truth}^{Weighted}} \div \frac{\Delta\phi_{Corr}}{\Delta\phi_{Truth}} \quad . \tag{5.4}$$

This distribution is taken as the associated systematic uncertainty due to the inaccuracies in the MC estimation of the third jet, and is included in figure 5.19.

5.3.3 Resolution

The final source of systematic error considered is the error associated with a mismodeling of the resolution of the detector in the GEANT4 simulation. In order to estimate this effect an over-smearing is applied. The analysis is redone using the nominal MC to obtain the unfolding correction. However, before the unfolding

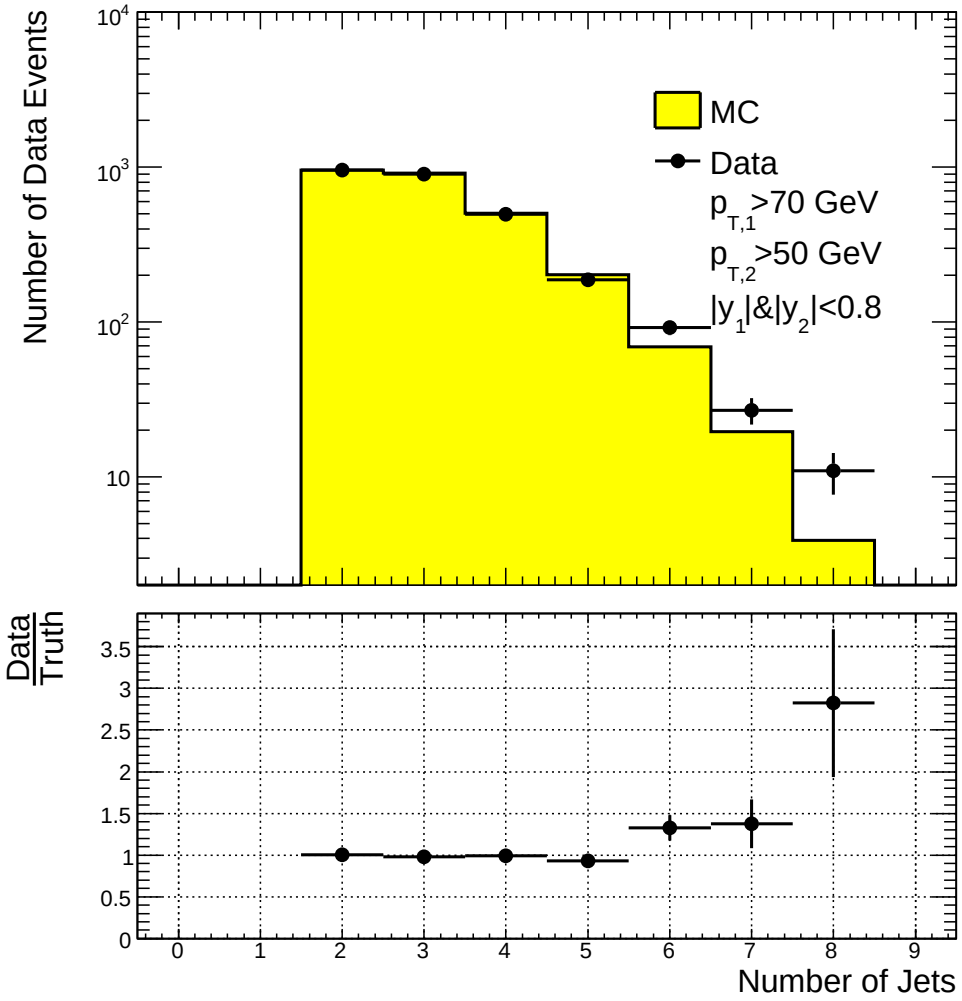

Figure 5.11: Number of jets. Ratio of data to full-sim Monte Carlo shown (lower).

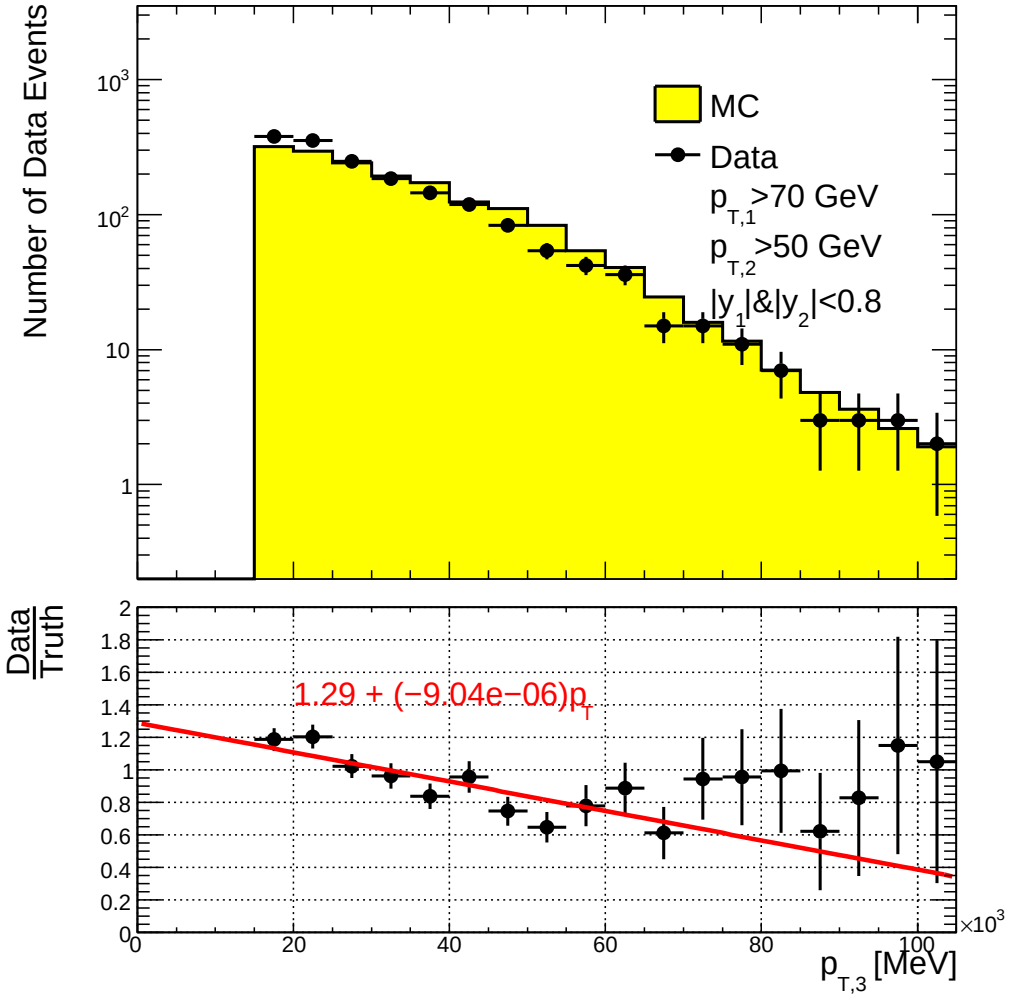

Figure 5.12: Distribution of third jet p_T. Ratio of data to full-sim Monte Carlo shown (lower).

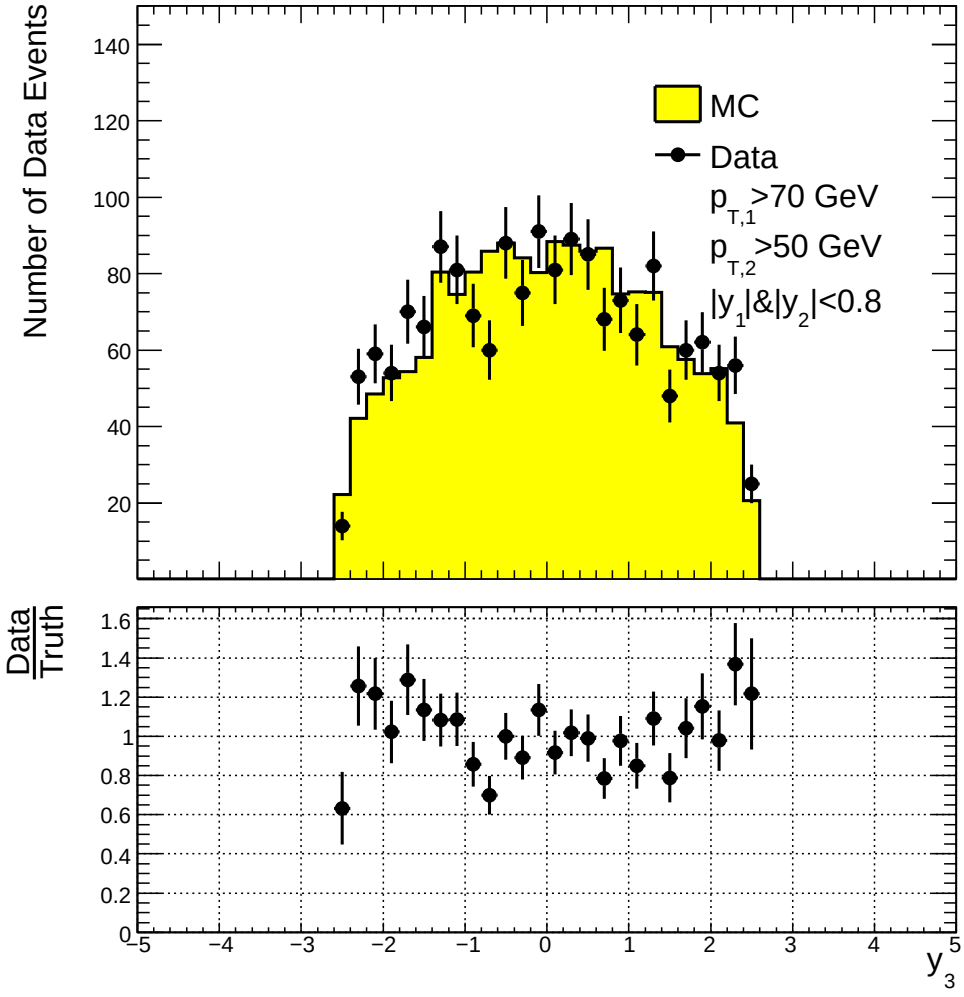

Figure 5.13: Distribution of third jet rapidity. Ratio of data to full-sim Monte Carlo shown (lower).

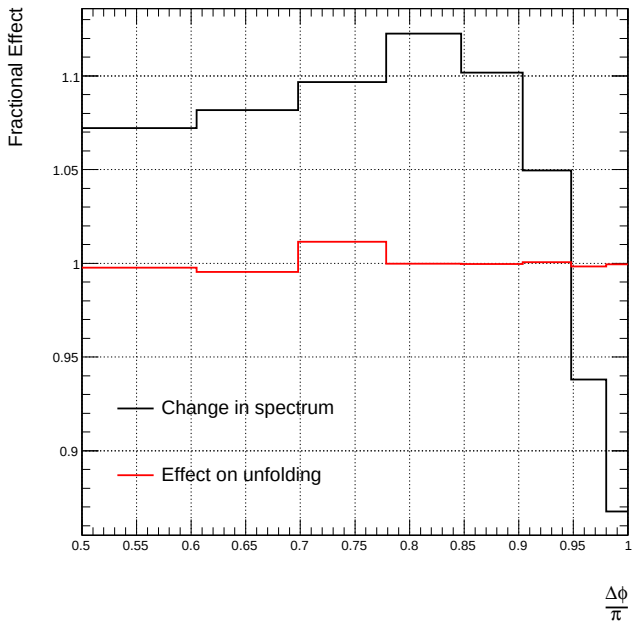

Figure 5.14: The effect of mis-modeled third jet kinematics: The red line shows the systematic error on the unfolding done using the a 3-D unfolding histogram, W. The black shows the effect on the $\Delta\phi$ spectrum of the weighting W_{jet3}.

correction is applied each (full-sim) jet has its p_T, η and ϕ smeared. If the variable being smeared is λ with a value of $\lambda = \lambda_0$ the smearing is done by shifting $\lambda_0 \rightarrow \lambda_0'$ where λ_0' is a random number chosen from a Gaussian distribution with mean λ_0 and width σ_λ^{smear}. In order to obtain a value for σ_λ^{smear}, first the p_T, η and ϕ resolutions as a function of p_T are estimated from from MC. To estimate the p_T resolution, for each truth jet, which is matched to a full-sim jet within $\Delta R < 0.4$ ($\Delta R = \sqrt{\Delta\phi + \Delta\eta}$), the p_T response ($\frac{p_T^{full-sim}}{p_T^{truth}}$) is calculated and histogrammed in bins of p_T^{truth}. The width of the each of these distributions is taken to be the relative resolution, i.e. $\frac{\sigma_{p_T}}{p_T}$ for that p_T bin. In order to find the width of the distribution a half-Gaussian, $G_{half}(\mu, \sigma)$, is fit to each bin's response distribution where the half-Gaussian is defined as

$$G_{half}(x) = A \times \theta(x - 1) \times G(1, \sigma) \tag{5.5}$$

where A is a normalization factor which is not used in the following, $\theta(x)$ is a Heavy-side Unit Step Function and $G(\mu, \sigma)$ is a Gaussian distribution with mean μ and width σ. For each bin the fit value $\sigma = \frac{\sigma_{p_T}}{p_T}$ is plotted versus the mean p_T value for that bin. Figure 5.15 shows the relative p_T resolution estimated from MC as a function of the truth jet p_T. Note that the half-Gaussian function is used, as opposed to a symmetric Gaussian, because of a bias at low p_T due to a cut in the minimum reconstructed jet p_T (which is 7 GeV). The points for a full Gaussian fit are overlaid in figure 5.15 as well and show a clear discrepancy at low p_T. Figure 5.16 shows an example bin at low p_T and one at higher p_T with both fits overlaid; note that at higher p_T the half-Gaussian and Gaussian functions have very similar widths. The

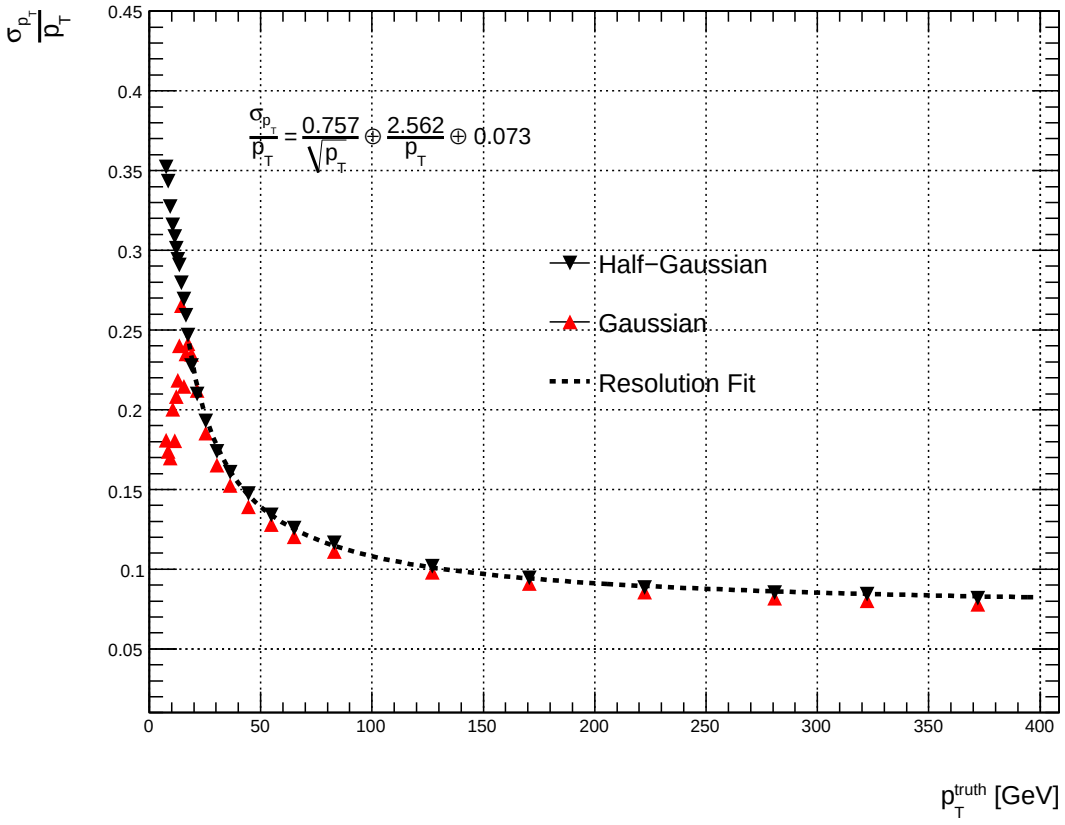

Figure 5.15: p_T resolution estimated from MC.

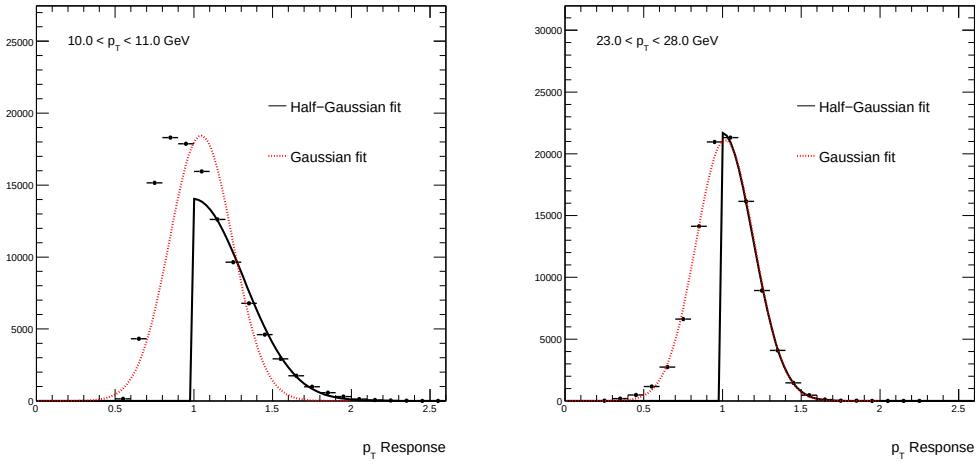

Figure 5.16: The half-Gaussian fit result to the p_T response in two example p_T bins.

$\frac{\sigma_{p_T}}{p_T}$ versus p_T plot is fit to the function

$$\left(\frac{\sigma_{p_T}}{p_T}\right)^2 = \left(\frac{a_1^2}{p_T} + a_2^2 + \frac{a_3^2}{p_T^2}\right) \tag{5.6}$$

where a_1, a_2 and a_3 are the fit parameters, giving the resolution as a function of p_T as

$$\sigma_{p_T} = p_T \left(\frac{a_1^2}{p_T} + a_2^2 + \frac{a_3^2}{p_T^2}\right)^{1/2} . \tag{5.7}$$

To obtain the resolutions for η and ϕ the same procedure is used however now the response is taken as an absolute response, $\eta^{full-sim} - \eta^{truth}$ and $\phi^{full-sim} - \phi^{truth}$ which makes the resolution as a function of p_T

$$\sigma = \left(\frac{a_1^2}{p_T} + a_2^2 + \frac{a_3^2}{p_T^2}\right)^{1/2} . \tag{5.8}$$

Where σ is either σ_η or σ_ϕ with the corresponding parameters a_1, a_2 and a_3 shown in table 5.2. The response distributions are fit to regular Gaussian functions not half-Gaussian functions. The resultant resolution plots are show in figures 5.17 and 5.18. The values of a_1, a_2 and a_3 for p_T, η and ϕ resolutions are listed in table 5.2.

With these parameterized resolution functions the value of σ_λ^{smear} (where λ represents p_T, η or ϕ) are taken as a fraction of the resolution, i.e. σ_λ^{smear} is taken as $\sigma \times \epsilon$ where σ is taken from equation 5.7 for p_T and equation 5.8 for η and ϕ. A preliminary result[44] for the discrepancy between the jet p_T resolution taken from MC and one derived from data shows agreement to within 15% for $|\eta < 2.8|$[33]* so ϵ is taken as 0.15 for the p_T over-smearing.

*This is intentionally a conservative estimate

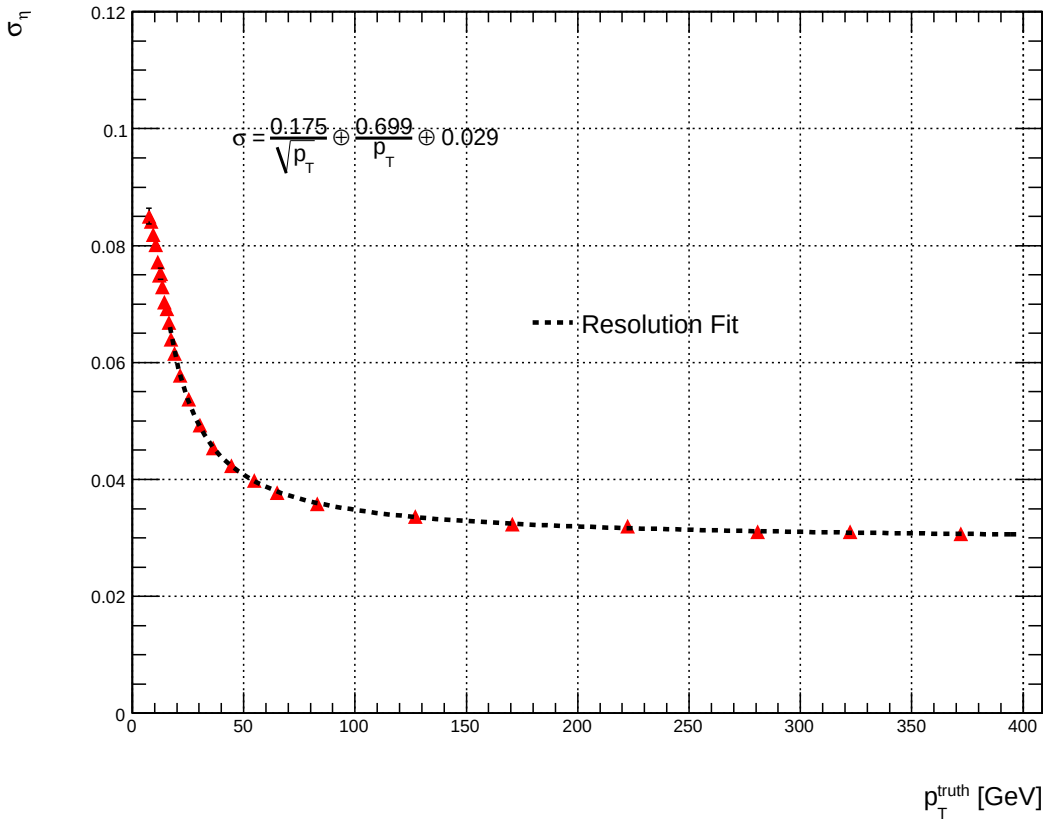

Figure 5.17: η resolution estimated from MC.

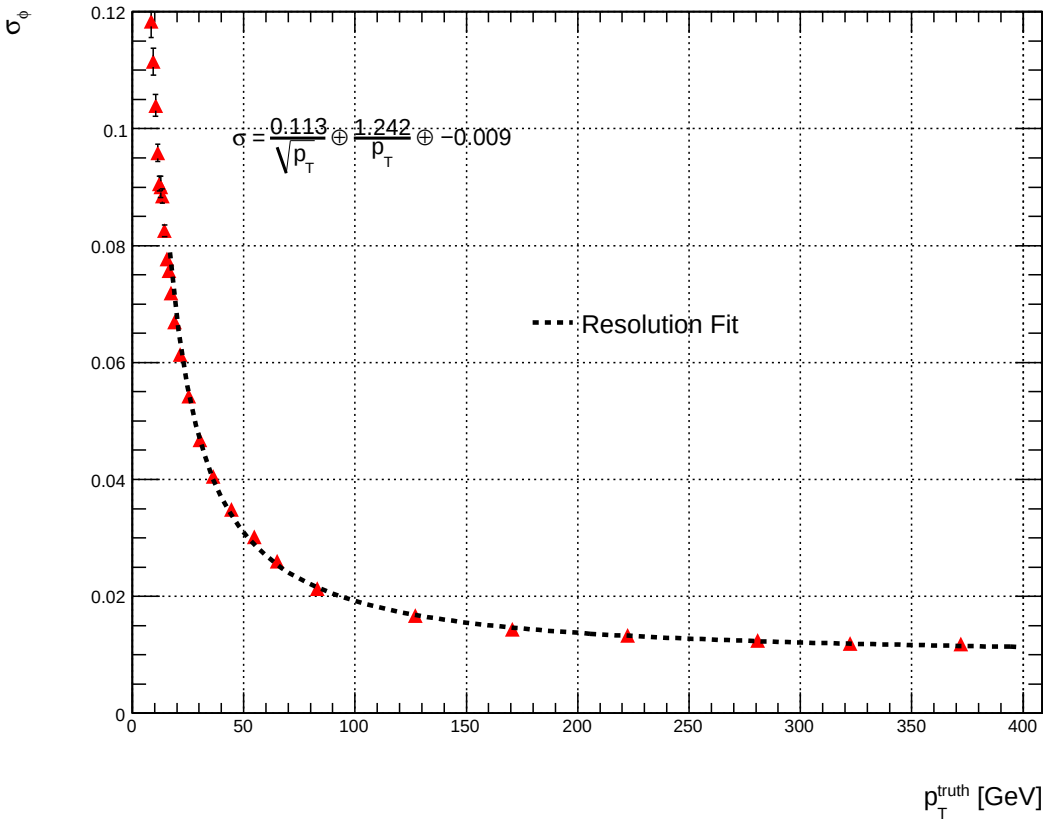

Figure 5.18: ϕ resolution estimated from MC.

Table 5.2: Jet resolution fit parameters and over smearing parameter ϵ_{smear}.

	a_1	a_2	a_3	ϵ_{smear}
p_T	0.757	2.56	0.07275	0.15
η	0.175	0.70	0.02926	0.10
ϕ	0.113	1.242	0.00935	0.05

Preliminary studies have been done[45] using an algorithm which matches tracks reconstructed by the inner detector to clusters in the calorimeters. This study looks at the width of the angular residual distributions and compares data and MC to quantify the magnitude of the discrepancy. The jet reconstruction is then run with the angular positions of the clusters smeared by this amount and the angular resolution effects are measured in the resulting jets. Conservative estimates for the effect on the jets are 10% and 5% for η and ϕ respectively, which give the corresponding values of ϵ of 0.1 and 0.05 shown in table 5.2.

Figure 5.19 shows the systematic error result for this over-smearing along with the systematic error estimates from all the other sources considered. The statistical error and total error are also shown.

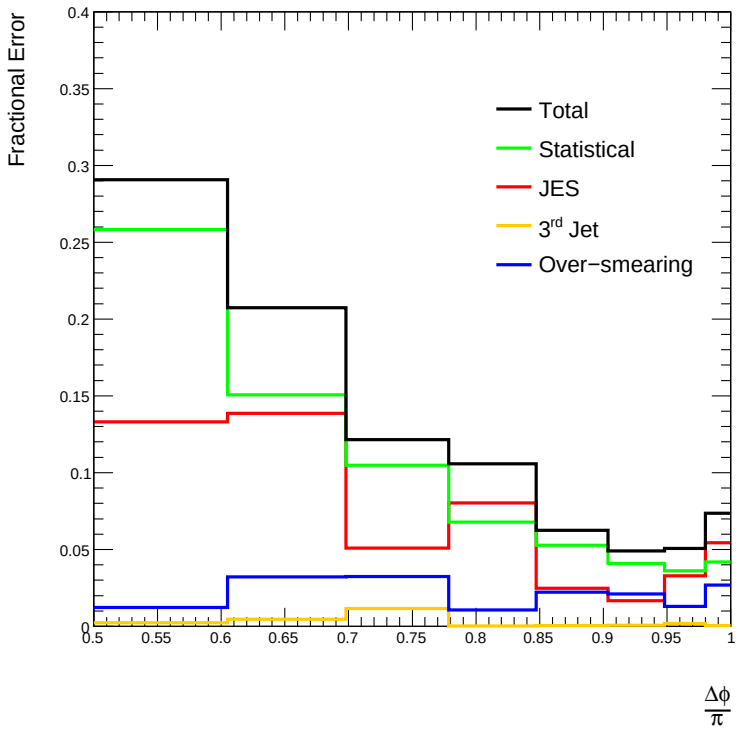

Figure 5.19: Relative systematic and statistical errors: All the sources of systematic errors are shown individually. The total error is taken as the quadratic sum of the individual errors.

Chapter 6

Result

The following chapter presents the unfolded normalized cross section $\frac{1}{\sigma_{tot}}\frac{d\sigma}{d(\Delta\phi)}$, plotted and tabulated showing statistical and systematic errors. A comparison to and a description of two MC event generators is also provided. The results are found in section 6.1 and the MC comparison and description are found in section 6.2.

6.1 Unfolded $\Delta\phi$ Spectrum

The final normalized $\Delta\phi$ spectrum after unfolding is shown in figure 6.1, which includes statistical and systematic errors. The numerical values for each point along with each source of uncertainty is detailed in table 6.1.

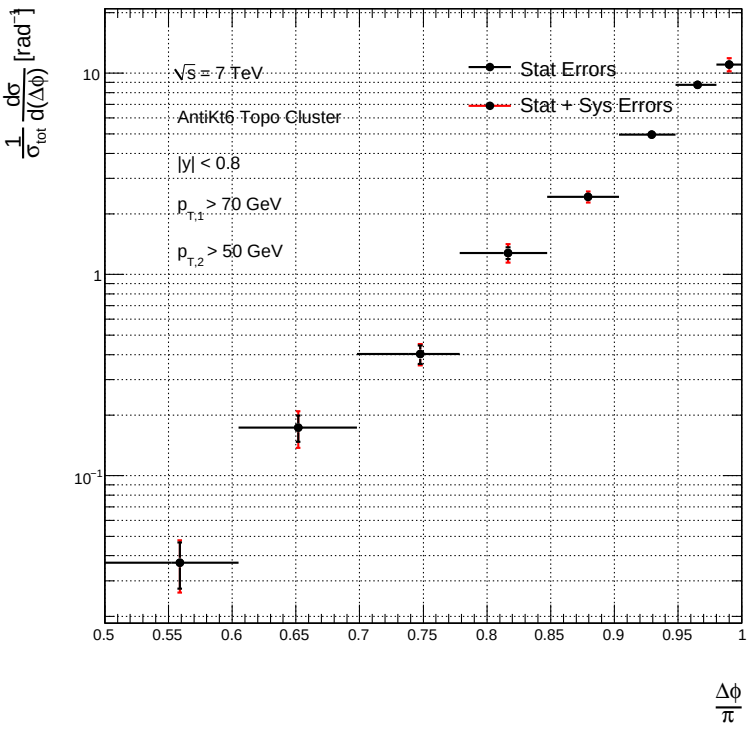

Figure 6.1: Unfolded normalized $\Delta\phi$ spectrum including statistical and systematic errors.

Table 6.1: Unfolded values of normalized $\Delta\phi$ spectrum including statistical and systematic errors.

Bin $[\frac{\Delta\phi}{\pi}]$	Average $[\frac{\Delta\phi}{\pi}]$	$\frac{1}{\sigma_{tot}}\frac{d\sigma}{d(\Delta\phi)}$	Stat Error [%]	Sys Error [%]	Total Error [%]
0.50-0.60	0.559	0.037	25.8	13.4	29.1
0.60-0.70	0.652	0.173	15.1	14.2	20.7
0.70-0.78	0.748	0.402	10.5	6.1	12.2
0.78-0.85	0.817	1.280	6.8	8.1	10.6
0.85-0.90	0.879	2.434	5.3	3.3	6.2
0.90-0.95	0.929	4.965	4.1	2.7	4.9
0.95-0.98	0.965	8.754	3.6	3.5	5.1
0.98-1.00	0.990	11.059	4.2	6.1	7.4

6.2 Comparison With Different Event Generators

Monte Carlo event generators are used to simulate high energy physics interactions. Given an initial state (here proton-proton collisions at centre of mass energy $\sqrt{s} = 7\,\text{TeV}$) the event generator is used to produce a large number of "events", which are a set of outgoing particles of known type and four momentum. The events are generated using a specific choice of interaction, or interactions (here $a+b \rightarrow X_{parton}$) where a and b are partons and X_{parton} is some partonic final state*. The two generators discussed below use the same basic concept of factorization as laid out in section 1.3 with some of the details explained in the following.

6.2.1 Pythia

The Pythia MC event generator[41] is a leading order (LO) event generator†. Pythia interfaces with CTEQ parton density functions[9] to model the parton distributions. The hard scattering parton-parton interaction is calculated to leading order only, i.e. $2 \rightarrow 2$ scattering of partons. A parton showering algorithm is then run to model multiple-parton final states and finally fragmentation is modelled. Note that the parton showering part would be included in the term $\hat{\sigma}_{ab\rightarrow X}$ of equation 1.2, that is, instead of this term being calculated exclusively from perturbative QCD, as was described earlier, it is calculated at LO by pQCD and then states with more partons are predicted not by higher order calculations, but rather by the parton showering

* "Final" state is a little misleading as it is not the final output of the event generator, but rather just the result of the hard parton-parton interaction.

† In fact Pythia does some NLO calculations but not for the processes of interest here.

model. The fragmentation, which involves modelling softer and collinear partons and hadronization, is modelled with the string fragmentation model.

The leading order calculation requires an energy scale, Q^2 to be set for the evaluation of the cross section. In Pythia calculations, this scale is chosen to be the transverse mass squared (m_T^2) of the outgoing partons. If the $2 \to 2$ process is $a + b \to c + d$ then

$$Q^2 = m_T^2 = \frac{1}{2}(m_c^2 + p_{T,c}^2 + m_d^2 + p_{T,d}^2) = \frac{1}{2}(m_c^2 + m_d^2) + \frac{\hat{t}\hat{u} - m_c^2 m_d^2}{\hat{s}} \tag{6.1}$$

where the Mandelstamm variables have been defined as: $\hat{s} = (p_c + p_d)^2$, $\hat{t} = (p_b + p_d)^2$ and $\hat{u} = (p_b + p_c)^2$. Or for the approximation of massless quarks

$$Q^2 = m_T^2 = \frac{\hat{t}\hat{u}}{\hat{s}} \, . \tag{6.2}$$

The parton showering model uses the probability of a "mother" parton (p_1) splitting into two "daughter" partons (p_2 and p_3), or $p_1 \to p_2 + p_3$ with parton p_2 taking momentum fraction z of p_1 and parton p_3 taking the remaining fraction, $1 - z$. After this splitting each of the partons p_2 and p_3 has the opportunity to be mothers themselves, and so on. The possible splittings considered are $q \to qg$, $g \to gg$ and $g \to q\bar{q}$ with probabilities derived using the splitting functions mentioned in section 1.3 to obtain what is referred to as the Sudakov form factor, which is the probability of p_1 NOT splitting into p_2 and p_3 after some time $t - t_0$ and is given by:

$$\mathcal{P}_{\text{no-splitting}}(t_0, t) = \exp\left(- \int_{t_0}^{t} dt' \sum_{2,3} \mathcal{I}_{23 \leftarrow 1}(t') \right) \tag{6.3}$$

where the summation over $2, 3$ is over all possible combination of pairs p_2 and p_3 and

$$\mathcal{I}_{23\leftarrow 1}(t) = \int_{z-t}^{z+t} dz \frac{\alpha_s}{2\pi} P_{23\leftarrow 1}(z) \tag{6.4}$$

where the P functions are the splitting functions. Note that the term "time" is a misnomer; it does not represent actual time, but instead represents an evolution variable which is given by

$$t = \ln\left(\frac{Q^2}{\Lambda^2}\right) \tag{6.5}$$

where Q is taken as the mass of the mother parton (m_1) and Λ is the scale above which pQCD is still applicable. Each pair of daughter partons is generated isotropically in the rest frame of the mother parton. This splitting is continued as long as $Q^2 > Q^2_{min}$ where, Q^2_{min} has a default value of $(1\,\mathrm{GeV})^2$. Once $Q \leq Q_{min}$ the parton does not split and is forced to be on mass shell. The evolution of t taking $Q = m_1$ is known as mass ordered parton showering.

As mentioned above, Pythia uses a string fragmentation model to evolve the partons resulting from the parton showering method described above into hadrons in the final state. The string model uses the analogy of outgoing partons connected via a string whose tension (κ) denotes the energy in the field between them. Pythia uses a model in which the string tension is a linear function of distance and is given a value of $\kappa = 1\,\mathrm{GeV/fm}$ or $0.2\,\mathrm{GeV}^2$. For example, consider the case of a quark anti-quark pair $q_0\bar{q}_0$ moving apart. Once there is sufficient energy in the string it can "break" producing another quark anit-quark pair $q_1\bar{q}_1$ leaving two strings, one between $q_0\bar{q}_1$ and one between $q_1\bar{q}_0$. Each string can then break again and again until what remains are only on-shell $q\bar{q}$ mesons. The probability of producing a "break" is related to a

tunnelling process for which the probability is

$$e^{\frac{-\pi m_{q,T}^2}{\kappa}} \tag{6.6}$$

where $m_{q,T}$ is the transverse mass of the quark such that $m_{q,T}^2 = m_q^2 + p_T^2$. The previous equation can then be factored giving

$$e^{\frac{-\pi m_q^2}{\kappa}} e^{\frac{-\pi p_T^2}{\kappa}} \tag{6.7}$$

which shows via the the quark mass dependance that there is a heavy quark suppression. The ratio of the production of quarks $u : d : s : c$ is approximately $1 : 1 : 0.3 : 10^{-11}$ strongly favouring the production of light quarks. The momentum fraction z taken by the hadron is obtained from a symmetric Lund fragmentation model:

$$f(z) \sim \frac{1}{z}(1-z)^2 e^{-\frac{bm_{h,T}^2}{z}} \tag{6.8}$$

where a and b are parameters which are determined empirically and $m_{h,T}$ is the hadron's transverse mass.

6.2.2 Herwig++

The Herwig++ event generator[30] is similar to the Pythia event generator with a few key differences, which are outlined below. Like Pythia, Herwig++ calculates at leading order, a $2 \rightarrow 2$ parton scattering followed by a parton shower. Here CTEQ PDFs are used as well. Herwig++, however, uses a different value for the Q^2 scale

for this evaluation. In Herwig++ the scale is chosen by

$$Q^2 = 2\frac{\hat{s}\hat{t}\hat{u}}{\hat{s}^2 + \hat{t}^2 + \hat{u}^2} \tag{6.9}$$

where $\hat{u}$, $\hat{t}$ and $\hat{u}$ again are the Mandelstamm variables.

The parton showering model in Herwig++ differs from that of Pythia with respect to the evolution of the variable t as defined in 6.5. In Herwig++ instead of using $Q^2 = m^2$, Q^2 is defined as

$$Q^2 = \frac{m^2}{z(1-z)} \tag{6.10}$$

where, here z is defined as the fractional momentum p_2 projected onto the direction of the mother particle's momentum p_1. This gives values of t which evolve according to the angular separation of the mother and daughter particles. This evolution scheme is known as angular ordering.

The hadronization model used in Herwig++ also differs to what is used in Pythia. Instead of a string fragmentation model, Herwig++ uses what is know as a cluster fragmentation model. This technique first converts outgoing gluons into quark anti-quark pairs, (or, with a lower probability, diquark anti-diquark). Then the (di)quarks are clustered with their nearest neighbours to form a colour singlet clusters. These clusters are then allowed to decay into hadrons. For a cluster of a quark anti-quark type $q_a\bar{q}_b$ the decay is performed by creating a quark anti-quark pair out of the vacuum, $q\bar{q}$, resulting in two hadrons $q_a\bar{q}$ and $q\bar{q}_b$.

The proceeding discussion was meant to be illustrative and does not explain the mechanism by which baryons can be produced by either Herwig++ or Pythia. Both

of these generators have such methods, descriptions of which can be found in the relevant references.

Figure 6.2 shows the unfolded $\Delta\phi$ spectrum with combined statistical and systematic errors, with the predictions of the Pythia and Herwig++ event generators overlaid. The Pythia tuning corresponds to the ATLAS default and the Herwig++ tuning corresponds to the default "out of the box" tuning of Herwig++.

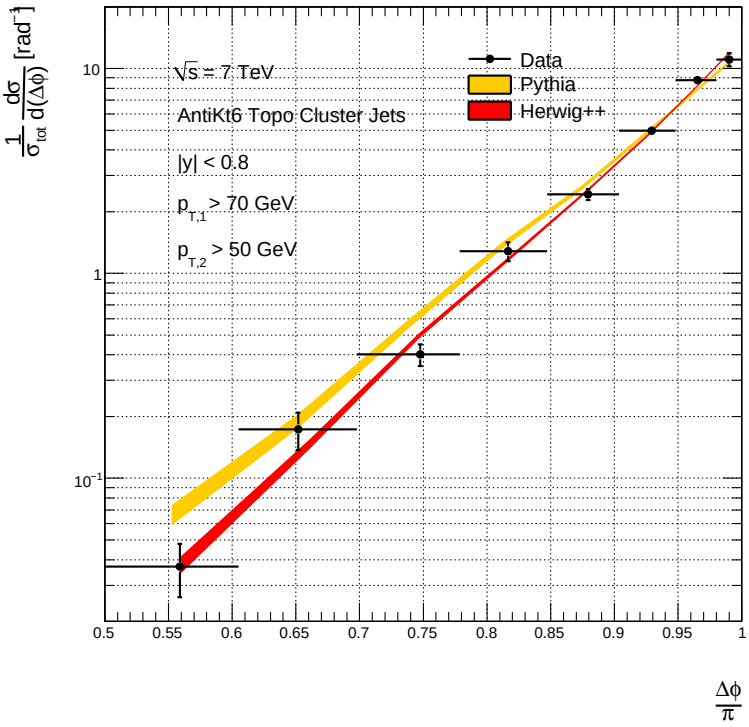

Figure 6.2: Unfolded normalized $\Delta\phi$ spectrum compared with Pythia and Herwig++ predictions.

Chapter 7

Conclusion

Using 19.55 nb^{-1} of proton-proton collision data at $\sqrt{s} = 7\,\mathrm{TeV}$ recorded between the 30 March and 4 June 2010 by the ATLAS detector at the Large Hadron Collider, the azimuthal decorrelation in di-jet events was studied by means of an observable, $\Delta\phi$ defined as the angle in the transverse plane between the two jets, with the highest transverse momenta in each event. A differential cross section, normalized by the inverse of total di-jet cross section was used in order to reduce additional uncertainties caused by efficiency effects and uncertainty on the total integrated luminosity. This observable was designed to be robust against systematic uncertainties resulting from detector effects, some of which may currently be large due to the fact that these data were recorded early in the running of the ATLAS experiment, while commissioning is still underway.

An unfolding procedure was performed on the $\Delta\phi$ spectrum using a Monte Carlo data set along with a GEANT4 simulation of the ATLAS detector including a simulation

of the full electronics chain. This unfolding procedure was performed in order to correct for effects in the measured spectrum which were due to the ATLAS detector. The result is a measurement which attempts to be independent of the detector from which it was made. The aim of this type of measurement is to allow for any other party to make a comparison with a similarly unfolded measurement from a different experiment, a jet level theory prediction, or a prediction from a Monte Carlo event generator.

The result has been compared to the predictions of two Monte Carlo event generators, Pythia 6.4.21 and Herwig++. The agreement with the Herwig++ simulated data was seen to be better than that to the Pythia simulated data. In a similar measurement made by the D0 collaboration [13] a comparison to Herwig[46] and Pythia also showed a better agreement between the Herwig prediction and data, although the Herwig and Pythia versions are not the same as was used in this analysis. All such types of event generators contain a large number of tuneable parameters which can be empirically determined from this type of measurement. The azimuthal decorrelation measurement made by the D0 collaboration has been used for MC event generator tuning[47, 48]. There has not yet been an attempt made to tune these parameters based on this result. The D0 measurement has also being compared to a next-to-leading-order calculation[49].

As the ATLAS detector records more and more data this measurement can and will be repeated with higher statistics, a better understanding of the detector and hence the jet properties and a higher range in jet energies.

Appendix A

Other Contributions to the ATLAS Experiment

The following section outlines some of the contributions I have made to the ATLAS experiment that were not mentioned in the preceding document.

A.1 General LAr Calibration and Commissioning

The ATLAS detector was installed underground at the LHC Point-1 between 2005 and 2008. Since this time (and even before the completed installation) much effort has been put into the commissioning of this detector. I have been involved in such efforts since first travelling to CERN in the summer of 2006. At this time groups of "experts" were formed in order to study the performance of the detector. I was involved at the first such expert week for the endcap calorimeters and have remained

involved since, becoming one of the earliest expert LAr shifters. The commissioning tasks were to prepare the detector for running once the LHC was operational. This involved taking shifts running calibration tests which were performed using electronic simulations of ionization pulses in the detector to calibrate and to find and diagnose problems in the detector's performance. The results of this work were summarized in [34], a paper of which I am an author.

Before the LHC was operational cosmic ray muons were used for detector commissioning as well. The data recorded during cosmic ray data taking was used to test the liquid argon's (as well as the rest of the detector's) trigger and data acquisition systems, electronics response and data processing capabilities. I was involved in data taking shifts as well as data analysis for the cosmic ray commissioning effort appeared as an author of two cosmic ray commissioning notes[50, 51].

A.2 LAr Endcap Calorimeter Noise Studies

Beyond the general calibration and commissioning tasks that were performed I was also charged with the task of studying the electronics noise and pedestals for the subdectectors in the liquid argon endcap region (these are the EMEC, HEC and FCal). My duties were to analyse calibration data in order to:

- quantify electronics noise channel by channel
- search for anomalies in the noise values and diagnose the cause
- develop tools to examine coherent noise in detectors and to diagnose the cause

and propose solutions

- monitor electronic pedestal values for stability and develop tools to do this in a automated fashion
- report findings to the liquid argon community

A.3 Hadronic Endcap Calibration Software

The software that was designed to process the raw calibration data from liquid argon detector tests was designed originally with the liquid argon barrel calorimeter in mind. For this reason certain aspects of the software were incompatible with the data output from the HEC. I was responsible for rewriting this software making it compatible with the HEC data while ensuring that it remained compatible with the all the other sub-detectors, thus allowing all LAr systems to use the same calibration software. This re-write affected all parts of the software chain, from the raw data level to the final GUI used to display results. These modifications allow the HEC calibration software to function and are part of the ATLAS software package.

A.4 Forward Calorimeter High Voltage Anomaly Modelling

The during installation of the FCal there was damage to one of the high voltage system which resulted in a region of the FCal having to be operated at a non-nominal

high voltage configuration. In order to better understand the effect of this I was in charge of adjusting the GEANT4 simulation of the FCal to incorporate this effect so that it could be accurately modelled in Monte Carlo data. I also used the output from the adjusted GEANT4 simulated data to study the effect on jet kinematics and to study the feasibility of a jet by jet correction. This software is now part of the official ATLAS software simulation package.

Bibliography

[1] J. Campbell, J.W. Huston, and W.J. Stirling. Hard Interactions of Quarks and Gluons: A Primer for LHC Physics. *Rept. Prog. Phys.*, 70:89, 2007.

[2] G. Salam. Towards Jetography. *Eur. Phys. J.*, C67:637–686, 2010.

[3] D. Griffiths. Introduction to elementary particles. *John Wiley and Sons*, 1987.

[4] M. Peskin and D. Schroeder. An introduction to quantum field theory. *Westview Press*, 1995.

[5] C. Burgess and G. Moore. The standard model: A primer. *Cambridge University Press*, 2007.

[6] C. Amsler et al. (Particle Data Group). *Physics Letters*, B667, 1, 2008.

[7] S. Bethke. The 2009 Wolrd Average of $\alpha_s(M_Z)$. *Eur. Phys. J.*, C64:689–703, 2009.

[8] J. Collins, D. E. Soper, and G. Sterman. Factorization for short distance hadron - hadron scattering. *Nucl. Phys.*, B261:104, 1985.

[9] P.M. Nadolsky et al. Implications of CTEQ global analysis for collider observables. *Phys. Rev.*, D78:013004, 2008.

[10] A. D. Martin, W. J. Stirling, R. S. Thorne, and G. Watt. Parton distributions for the LHC. *Eur. Phys. J.*, C63:189–285, 2009.

[11] G. Altarelli and G. Parisi. Asymptotic freedom in parton language. *Nucl. Phys.*, B126:298, 1977.

[12] Durham HEP Databases. Parton Distribution Server. *http://durpdg.dur.ac.uk/hepdata/pdf.html*.

[13] V.M. Abazov et al. Measurement of dijet azimuthal decorrelations at central rapidities in p-p collisions at $\sqrt{s} = 1.96\,\text{TeV}$. *Phys. Rev. Lett.*, 94(22):221801, 2005.

[14] G. Aad et al. The ATLAS Experiment at the CERN Large Hadron Collider. *JINST*, 3:S08003, 2008.

[15] ATLAS Collaboration. Atlas detector and physics performance: Technical design report, 1. 1999.

[16] G. Aad et al. Expected Performance of the ATLAS Experiment - Detector, Trigger and Physics. 2009.

[17] L. Evans, (ed.) and P. Bryant, (ed.). LHC Machine. *JINST*, 3:S08001, 2008.

[18] M. Banner et al. Observation of single isolated electrons of high transverse momentum in events with missing transverse energy at the CERN anti-p p collider. *Phys. Lett.*, B122:476–485, 1983.

[19] G. Arnison et al. Experimental observation of lepton pairs of invariant mass around 95-GeV/c**2 at the CERN SPS collider. *Phys. Lett.*, B126:398–410, 1983.

[20] G. Montagna, O. Nicrosini, and F. Piccinini. Precision physics at LEP. *Riv. Nuovo Cim.*, 21N9:1–162, 1998.

[21] C. Campagnari and M. Franklin. The discovery of the top quark. *Rev. Mod. Phys.*, 69(1):137–212, 1997.

[22] C. Mariotti. Search of the standard model Higgs at LEP. *Nuclear Physics B - Proceedings Supplements*, 117(Supplement 1):202 – 205, 2003.

[23] G. Flugge. Future Research in High Energy Physics. *1993 European School of High Energy Physics, Yellow reports*, CERN 94-04, 1994.

[24] G. Aad et al. Performance of the minimum bias trigger in p-p collisions at $\sqrt{s} = 7\,\text{TeV}$. Technical Report ATL-CONF-2010-068, CERN, Geneva, 2010.

[25] K. Jon-And. Status of the ATLAS Experiment. Technical Report ATL-GEN-PROC-2010-001, ATL-COM-GEN-2010-003, CERN, Geneva, 2010.

[26] W. Lampl et al. Calorimeter clustering algorithms: Description and performance. Technical Report ATL-LARG-PUB-2008-002, ATL-COM-LARG-2008-003, CERN, Geneva, 2008.

[27] M. Cacciari, G. Salam, and G. Soyez. The anti-k_T jet clustering algorithm. *JHEP*, 04:063, 2008.

[28] S. Catani, Yuri L. Dokshitzer, M. H. Seymour, and B. R. Webber. Longitudinally invariant K_t clustering algorithms for hadron hadron collisions. *Nucl. Phys.*, B406:187–224, 1993.

[29] L. Asquith et al. Performance of jet algorithms in the atlas detector. Technical Report ATL-COM-PHYS-2009-630, CERN, Geneva, 2009.

[30] M. Bahr et al. Herwig++ Physics and Manual. *Eur. Phys. J.*, C58:639–707, 2008.

[31] ATLAS Public Results: Event Displays. *https://twiki.cern.ch/twiki/bin/view/Atlas/EventDisplayPublicResults*.

[32] D. Lopez Mateos, E.W. Hughes, and A. Schwartzman. A simple p_t- and η-dependent monte carlo-based jet calibration. Technical Report ATL-COM-PHYS-2009-076, CERN, Geneva, 2009.

[33] M. Bagel et al. Jet energy scale and its systematic uncertainty for jets produced in proton-proton collisions at $\sqrt{s} = 7\,\text{TeV}$ and measured with the ATLAS detector. Technical Report ATLAS-CONF-2010-056, CERN, Geneva, 2010.

[34] G. Aad et al. Readiness of the ATLAS liquid argon calorimeter for LHC collisions. Dec 2009.

[35] J. M. Abdallah et al. ATLAS tile calorimeter data quality assessment with commissioning data. *J. Phys. Conf. Ser.*, 119:032001, 2008.

[36] ATLAS Run Query tool. *http://atlas-runquery.cern.ch/*.

[37] S. van dar Meer. Calibration of the effective beam height in the ISR, CERN-ISR-PO-68-31. (CERN-ISR-PO-68-31), 1968.

[38] D. Berge, A. Hoecker, A. Messina, and G. Piacquadio. Determination of the absolute luminosity and the visible cross section from LHC van der Meer scans using events with MBTS triggers and with primary vertices. Technical Report ATL-COM-LUM-2010-023, CERN, Geneva, 2010.

[39] B. Demirkoz, M. Martinez, and E. Meoni. Measurement of level1 jet trigger efficiencies in ATLAS using pp minimum bias data at $\sqrt{s} = 7\,\text{TeV}$. Technical Report ATL-COM-DAQ-2010-114, CERN, Geneva, 2010.

[40] M. Baak, M. Petteni, and N. Makovec. Data-quality requirements and event cleaning for jets and missing transverse energy reconstruction with the atlas

detector in proton-proton collisions at a center-of-mass energy of $\sqrt{s} = 7\,\text{TeV}$. Technical Report ATLAS-COM-CONF-2010-038, CERN, Geneva, 2010.

[41] T. Sjostrand, S. Mrenna, and P.Z. Skands. PYTHIA 6.4 physics and manual. *JHEP*, 05:026, 2006.

[42] S. Agostinelli et al. GEANT4 - a simulation tool kit. *Nucl. Instrum. Methods*, A506:238, 2001.

[43] G. Aad et al. The ATLAS simulation infrastructure. *arXiv:1005.4568*, 2010.

[44] K. Perez, G. Romeo, and A. Schwartzman. Jet energy resolution and reconstruction efficiencies from in-situ techniques with the ATLAS detector using proton-proton collisions at a center of mass energy $\sqrt{s} = 7\,\text{TeV}$. Technical Report ATL-COM-PHYS-2010-409, CERN, Geneva, 2010.

[45] S. Majewski et al. Dijet $\Delta\phi$ decorrelation studies for HCP (SM physics group presentation). *http://indico.cern.ch/contributionDisplay.py?contribId=4&confId=100793*, 2010.

[46] G. Corcella et al. HERWIG 6.5: an event generator for hadron emission reactions with interfering gluons (including supersymmetric processes). *JHEP*, 01:010, 2001.

[47] J. M. Butterworth et al. The tools and monte carlo working group summary report. 2010.

[48] P. Z. Skands. The perugia tunes. 2010.

[49] J. M. Butterworth. Quantum chromodynamics at colliders. *Int. J. Mod. Phys.*, A21:1792–1804, 2006.

[50] H. Okawa et al. Calorimeter commissioning with cosmic rays: cells, clusters, jets and missing ET. Technical Report ATL-COM-CAL-2008-007, CERN, Geneva, 2008.

[51] R. Teuscher et al. Fake missing transverse energy from ATLAS calorimeter cosmic ray data. Technical Report ATL-COM-CAL-INT-2008-001, CERN, Geneva, 2008.